

Differentiation of Hypertrophic Chondrocytes from Human iPSCs for the *In Vitro* Modeling of Chondrodysplasias

Yann Pretemer,¹ Shunsuke Kawai,^{1,2,3} Sanae Nagata,¹ Megumi Nishio,² Makoto Watanabe,^{1,4} Sakura Tamaki,^{2,5} Cantas Alev,^{1,6} Yoshihiro Yamanaka,^{1,6} Jing-Yi Xue,⁷ Zheng Wang,^{7,8} Kenichi Fukiage,^{9,10} Masako Tsukanaka,⁹ Tohru Futami,⁹ Shiro Ikegawa,⁷ and Junya Toguchida^{1,2,3,5,*}

¹Department of Cell Growth and Differentiation, Center for iPS Cell Research and Application, Kyoto University, Kyoto, Japan

²Department of Regeneration Science and Engineering, Institute for Frontier Life and Medical Sciences, Kyoto University, Kyoto, Japan

³Department of Orthopaedic Surgery, Graduate School of Medicine, Kyoto University, Kyoto, Japan

⁴Life Science Research Center, Technology Research Laboratory, Shimadzu Corporation, Kyoto, Japan

⁵Institute for Advancement of Clinical and Translational Sciences, Kyoto University Hospital, Kyoto University, Kyoto, Japan

⁶Institute for the Advanced Study of Human Biology, Kyoto University, Kyoto, Japan

⁷Laboratory for Bone and Joint Diseases, RIKEN Center for Integrative Medical Sciences, Tokyo, Japan

⁸McKusick-Zhang Center for Genetic Medicine and State Key Laboratory of Medical Molecular Biology, Institute of Basic Medical Sciences, Chinese Academy of Medical Sciences & Peking Union Medical College, Beijing, China

⁹Department of Pediatric Orthopaedics, Shiga Medical Center for Children, Moriyama, Japan

¹⁰Department of Orthopaedic Surgery, Bobath Memorial Hospital, Osaka, Japan

*Correspondence: togjun@cira.kyoto-u.ac.jp

<https://doi.org/10.1016/j.stemcr.2021.01.014>

SUMMARY

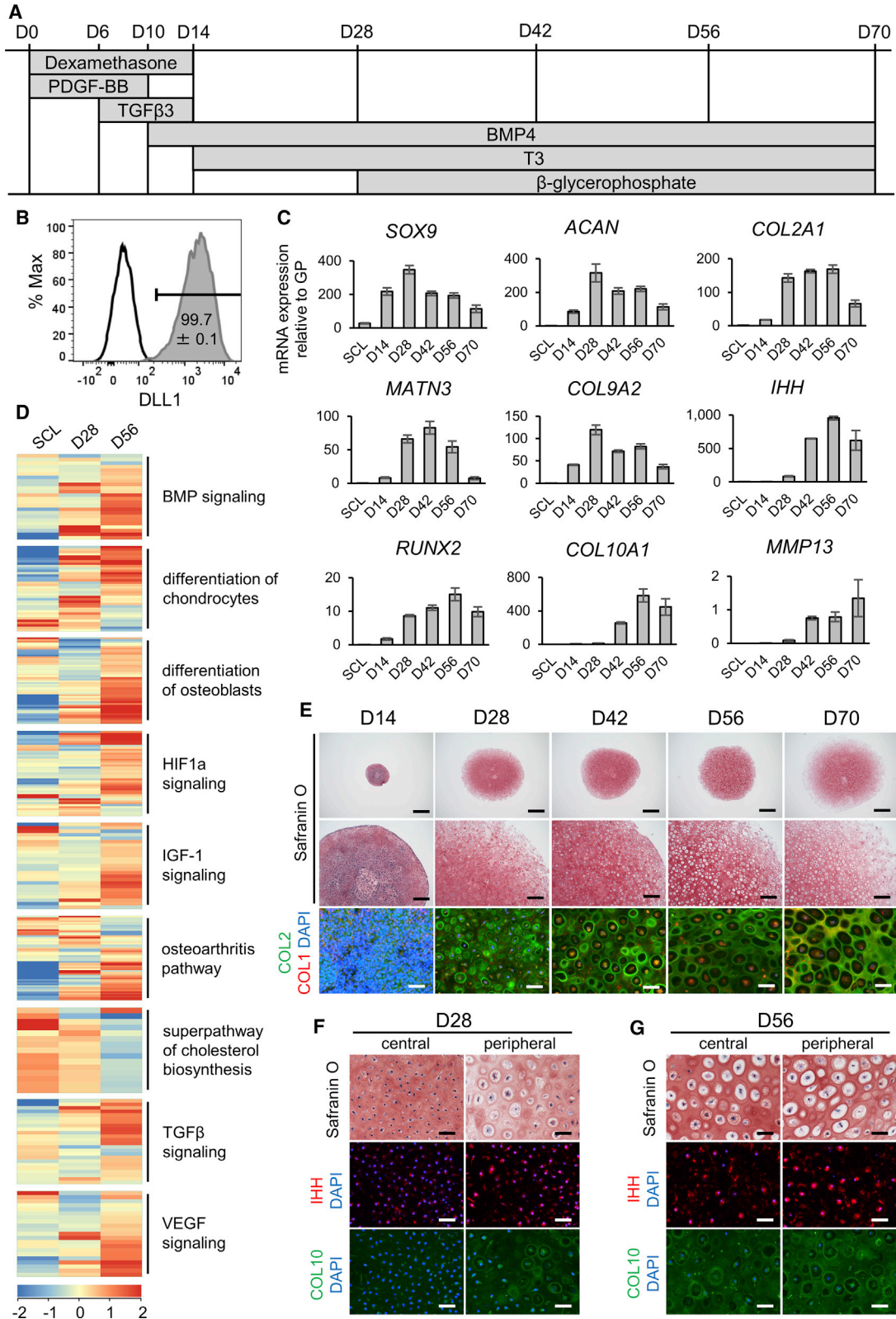
Chondrodysplasias are hereditary diseases caused by mutations in the components of growth cartilage. Although the unfolded protein response (UPR) has been identified as a key disease mechanism in mouse models, no suitable *in vitro* system has been reported to analyze the pathology in humans. Here, we developed a three-dimensional culture protocol to differentiate hypertrophic chondrocytes from induced pluripotent stem cells (iPSCs) and examine the phenotype caused by *MATN3* and *COL10A1* mutations. Intracellular *MATN3* or *COL10* retention resulted in increased ER stress markers and ER size in most mutants, but activation of the UPR was dependent on the mutation. Transcriptome analysis confirmed a UPR with wide-ranging changes in bone homeostasis, extracellular matrix composition, and lipid metabolism in the *MATN3* T120M mutant, which further showed altered cellular morphology in iPSC-derived growth-plate-like structures *in vivo*. We then applied our *in vitro* model to drug testing, whereby trimethylamine N-oxide led to a reduction of ER stress and intracellular *MATN3*.

INTRODUCTION

Chondrodysplasias are hereditary cartilage disorders, which often manifest by early childhood as mild to severe skeletal abnormalities due to mutations in the components of growth cartilage. In multiple epiphyseal dysplasia (MED; OMIM #607078) and metaphyseal chondrodysplasia type Schmid (MCDS; OMIM #156500), short-limbed dwarfism and deformities of the hips or knees are commonly observed (Czarny-Ratajczak et al., 2001; Mäkitie et al., 2005), but large variations in the skeletal phenotype and disease severity between patients have made these diseases difficult to research and treat. To overcome the obstacles posed by this heterogeneity and deepen our understanding of chondrodysplasias, it is imperative to obtain relevant patient samples and establish accurate disease models.

However, as it is ethically questionable to obtain samples from patients' growth plates, much of our understanding of chondrodysplasia disease mechanisms has come from studies of animal models. Mutations in the *MATN3* vWfa and *COL10A1* NC1 domains, which respectively cause MED and MCDS, have been reported to disrupt folding and oligomerization *in vitro* (Cotterill et al., 2005; Wilson et al., 2005), suggesting a gain-of-function effect that has

been further supported by *Matn3* or *Col10a1* knockout mice having no significant skeletal dysplasia (Kwan et al., 1997; van der Weyden et al., 2006). In contrast, model mice with the p.V194D mutation in *Matn3*, known to cause MED in humans, showed short-limbed dwarfism and structural disruption of the growth plate with decreased chondrocyte proliferation and increased apoptosis (Leighton et al., 2007). Similarly, model mice with the MCDS-causing p.N617K mutation in *Col10a1* also showed short-limbed dwarfism, but the growth plate had an extended hypertrophic zone without decrease in chondrocyte proliferation (Rajpar et al., 2009). In both models, ER stress was detected in growth plate chondrocytes as a result of intracellular accumulation of *MATN3* or *COL10*, indicating that the unfolded protein response (UPR) is a key event in these diseases. However, these results were obtained using homozygous mice, while most MED- and MCDS-causing mutations are heterozygous with autosomal dominant inheritance in humans (Mortier et al., 2019). Of the heterozygous mouse models, only the *COL10A1* Y632X heterozygotes demonstrated a clear phenotype (Forouhan et al., 2018), but contrary to this model, where the mutant Y632X mRNA was stable, human cartilage cells with an identical mutation showed no mRNA transcripts from the mutant allele (Chan et al.,



(legend on next page)



1998), suggesting that haploinsufficiency may be causative in humans. Due to these species differences, models that more closely reflect the pathology in humans are required.

Recently, disease-specific induced pluripotent stem cells (iPSCs) have emerged as a powerful tool to further our understanding of human hereditary diseases and screen for candidate drugs. For example, the clinical phenotype of type II collagenopathies, a subgroup of chondrodysplasias, has been recapitulated *in vitro* using patient-derived iPSCs (Okada et al., 2015). Therefore, in this study, we aimed to apply this approach to MED and MCDS. As these two chondrodysplasias mainly or partly affect hypertrophic chondrocytes, we first developed a three-dimensional (3D) culture protocol to robustly derive such late-stage chondrocytes. Then, using both patient-derived and artificially mutated iPSC lines with heterozygous *MATN3* or *COL10A1* mutations, we applied our protocol to the *in vitro* recapitulation of MED and MCDS phenotypes. Comparison with isogenic controls enabled us to demonstrate a phenotype in some mutants that is similar to previous observations in model mice, including ER stress and a UPR caused by the intracellular accumulation of the affected protein, indicating the usefulness of our model for the analysis of diseases affecting the growth plate. However, evidence of ER stress and the UPR was weaker in other mutants, suggesting that each mutation, even in the same causative gene, may have a different impact on the phenotype. Our system provides an initial platform for further investigation and drug development of growth plate diseases.

RESULTS

Differentiation of iPSCs into hypertrophic chondrocytes through the sclerotome

To model chondrodysplasias *in vitro*, we first developed a protocol of differentiating hypertrophic chondrocytes from the wild-type 414C2 iPSC line (Okita et al., 2011) in

serum-free conditions. We combined previously reported protocols of sclerotome induction (Matsuda et al., 2020) and chondrogenic induction (Umeda et al., 2012) with slight modifications. After sclerotome induction (SI), hypertrophic chondrocyte induction (HI) was performed in 3D culture for up to 70 days, starting with a 14-day-period of standard chondrogenic induction (Umeda et al., 2012) before adding the thyroid hormone T3, which has been reported to promote hypertrophic maturation (Mueller and Tuan, 2008) (Figure 1A).

This protocol required no cell sorting, as fluorescence-activated cell sorting (FACS) analysis at the presomitic mesoderm (PSM) stage during SI showed that almost 100% of cells were positive for the PSM marker DLL1 (Figure 1B). The expression of chondrocyte markers was detected from day 14 of HI, peaking on day 28 and declining thereafter, while hypertrophic markers mostly appeared on day 42, with an expression similar to or greater than the human distal femoral growth plate (Figure 1C). Transcriptome and Ingenuity Pathway Analysis (IPA) of day-56 pellets compared with day-28 pellets showed gene expression changes in several chondrocyte hypertrophy-related pathways, including increases in bone morphogenetic protein (BMP) and insulin-like growth factor-1 (IGF-1) signaling (Karl et al., 2014; Wang et al., 1999) and decreases in cholesterol biosynthesis (Tsushima et al., 2018) (Figure 1D and Table S1). Apart from these pathways, both chondrocyte and osteoblast differentiation-related gene expression were increased as the chondrocytes matured from sclerotome until day 56.

The pellet dramatically increased in size from 1 mm on day 14 to 4–5 mm on day 28, stabilizing thereafter (Figure 1E). The cartilage matrix stained with Safranin O by day 14, COL2 by day 28, and COL1 by day 70. On day 28, cells resembled proliferating chondrocytes in the pellet interior, with only a thin layer of cells with a hypertrophic morphology in the periphery of the pellet, but by day 56 a hypertrophic morphology was detected throughout the

Figure 1. Differentiation of hypertrophic chondrocytes from iPSCs

- (A) Protocol of hypertrophic chondrocyte induction (HI) in 3D pellet culture from sclerotome (SCL) cells (D0).
(B) Representative result of DLL1-positive cells (compared with isotype control) on day 2 of sclerotome induction (SI), with the mean and SEM (standard error of the mean) of $n = 4$ independent experiments displayed.
(C) mRNA expression of chondrocyte markers of different stages over time from SCL on day -1 to day 70 of HI by qPCR (top row, early markers; middle row, proliferating to prehypertrophic markers; bottom row, hypertrophic markers). Values are shown as mean \pm SEM ($n = 4$ independent experiments), relative to the mean of six pieces of a human distal femoral growth plate (GP).
(D) Heatmap of averaged normalized intensity values of gene expression in chondrocyte hypertrophy-related pathways from IPA in SCL, day-28, and day-56 samples ($n = 3$ independent experiments).
(E) Safranin O staining (top and middle rows) and COL2 (green) with COL1 (red) immunostaining (bottom row) of pellets from days 14–70 of HI. Scale bars, 1 mm (top row), 200 μ m (middle row), 50 μ m (bottom row).
(F and G) Safranin O and IHH or COL10 immunostaining on day 28 (F) and day 56 (G) of HI in the central or peripheral area of each pellet. Scale bars, 50 μ m.

All results shown are from experiments using the 414C2 wild-type iPSC line. For (E), (F), and (G), similar results were obtained in $n = 3$ independent experiments. See also Figure S1 and Table S1.



pellet. Prehypertrophic marker *IHH* and hypertrophic marker *COL10* were present at a higher level in the peripheral area than the central area on day 28, further increasing in both areas by day 56 (Figures 1F and 1G). The expression of chondrocyte markers and the change in chondrocyte morphology during HI were similar in the 1231A3 iPSC line (Nakagawa et al., 2014) (Figures S1A–S1E). Markers of other tissues, such as adipose and ligament, were not expressed at high levels throughout the induction, but markers of bone, including *IBSP* and *SP7*, increased as chondrocytes moved toward hypertrophy (Figure S1F). Together with *COL1* staining on day 70, this suggests some cells may also have differentiated into the osteoprogenitor lineage in the later stages.

Patient analysis and establishment of *COL10A1* and *MATN3* mutant iPSC lines

iPSC lines were established from one MED patient with a previously reported heterozygous *MATN3* c.359C>T (p.T120M) mutation (Jackson et al., 2004), one MCDS patient with a novel heterozygous *COL10A1* c.1841_1841delT (p.L614Rfs*8) mutation, and one MCDS patient with a previously reported heterozygous *COL10A1* c.53G>A (p.G18E) mutation (Ikegawa et al., 1997). Karyotype analysis showed no chromosomal abnormalities in the two clones from each patient (Figures S2A, S3A, and S4A). Each clone showed normal morphology, the presence of pluripotency markers, and the ability to differentiate into all three germ layers (Figures S2B–S2E, S3B–S3E, and S4B–S4E).

Radiological findings in the MED patient included bowing of the femora with genu varum, as well as mild platyspondyly and scoliosis (Figure S2F). The patient's height at age 9 years was 2.2 SD (standard deviations) below normal. The *MATN3* T120M mutation was corrected in the rescued clone (Figure S2G). In addition to the *MATN3* T120M mutation, the SNP *MATN3* c.659T>C (p.V220A), which has been reported in both MED patients and normal controls (Kim et al., 2011), was also detected in the MED patient's healthy allele (Figure S2H). To further analyze the pathology of *MATN3* mutations, we created a heterozygous *MATN3* c.626G>C (p.R209P) mutation in 414C2 iPSCs (Figure S2I). This mutation has been previously reported in MED, causing genu valgum but no dwarfism (Kim et al., 2011).

MCDS patient #1, who had the *COL10A1* L614Rfs*8 mutation, showed a typical MCDS phenotype by age 2 years, with radiological findings including metaphyseal flaring and coxa vara (Figure S3F). The mutation was corrected in the rescued clone (Figure S3G). Despite the early stop codon resulting from the frameshift mutation, nonsense-mediated decay (NMD) was not detected (Figure S3H). MCDS patient #2, with the *COL10A1* G18E mutation,

has been previously described with radiological findings including widening of the physes, bowing of the femora, and coxa vara (Ikegawa et al., 1997). The mutation was corrected in the rescued clone (Figure S4F). Another heterozygous *COL10A1* mutant with the c.1798T>C (p.S600P) mutation was created using 414C2 iPSCs (Figure S4G). This mutation has been reported in an MCDS patient with short-limbed dwarfism, coxa vara, and metaphyseal abnormalities (Gregory et al., 2000). Sequencing of cDNA reverse transcribed from RNA showed that mutant RNA is present in all mutants (Figures S2J, S2K, S3I, S4H, and S4I).

COL10A1 and *MATN3* mutants differentiate into hypertrophic chondrocytes

We next assessed the ability of our mutant iPSC lines to differentiate into hypertrophic chondrocytes. At the PSM stage, mutants showed an equal or higher percentage of DLL1-positive cells (Figure 2A). On day 56 of HI, the expression of chondrocyte markers from various stages was, with some clonal variation, similar in mutants and isogenic controls (Figure S5A). However, some mutants showed a lower expression of *IHH*, which is part of the *IHH*-PTHrP feedback loop that regulates chondrocyte differentiation in the growth plate (Kobayashi et al., 2002), suggesting a possible disruption in the signaling that regulates chondrocyte maturation. *MATN3* expression in *MATN3* mutants was unchanged, but *COL10A1* expression decreased in the *COL10A1* S600P mutant (Figure 2B). Cartilage matrix production was not disrupted in mutants, as Safranin O, COL2, and COL1 staining, as well as the pellet size, were similar to that in isogenic controls (Figures 2C–2G and S5B). Despite the changes in *IHH* and *COL10A1* expression, the cell morphology was not different between mutants and controls, with both showing a hypertrophic morphology. The cell size showed no consistent changes for *COL10A1* or *MATN3* mutants and, surprisingly, cell death was unchanged or actually decreased in mutants (Figures 2H and 2I).

COL10 or *MATN3* is retained intracellularly in mutants

Since MCDS and MED model mice accumulate the mutated protein intracellularly, we examined whether this is also the case in humans. Indeed, immunostaining of the protein on day 56 of HI revealed the presence of intracellular aggregates in both *COL10A1* and *MATN3* mutants (Figures 3A, 3B, S5C, and S5D). These aggregates co-stained with the ER marker PDI, showing that they are retained within the ER. At the same time, extracellular COL10 or MATN3 was decreased in mutants. All mutants showed a significant increase of COL10 or MATN3 retention, which differed depending on the mutation and was particularly elevated in the *MATN3* T120M mutant (Figures 3C and 3D).

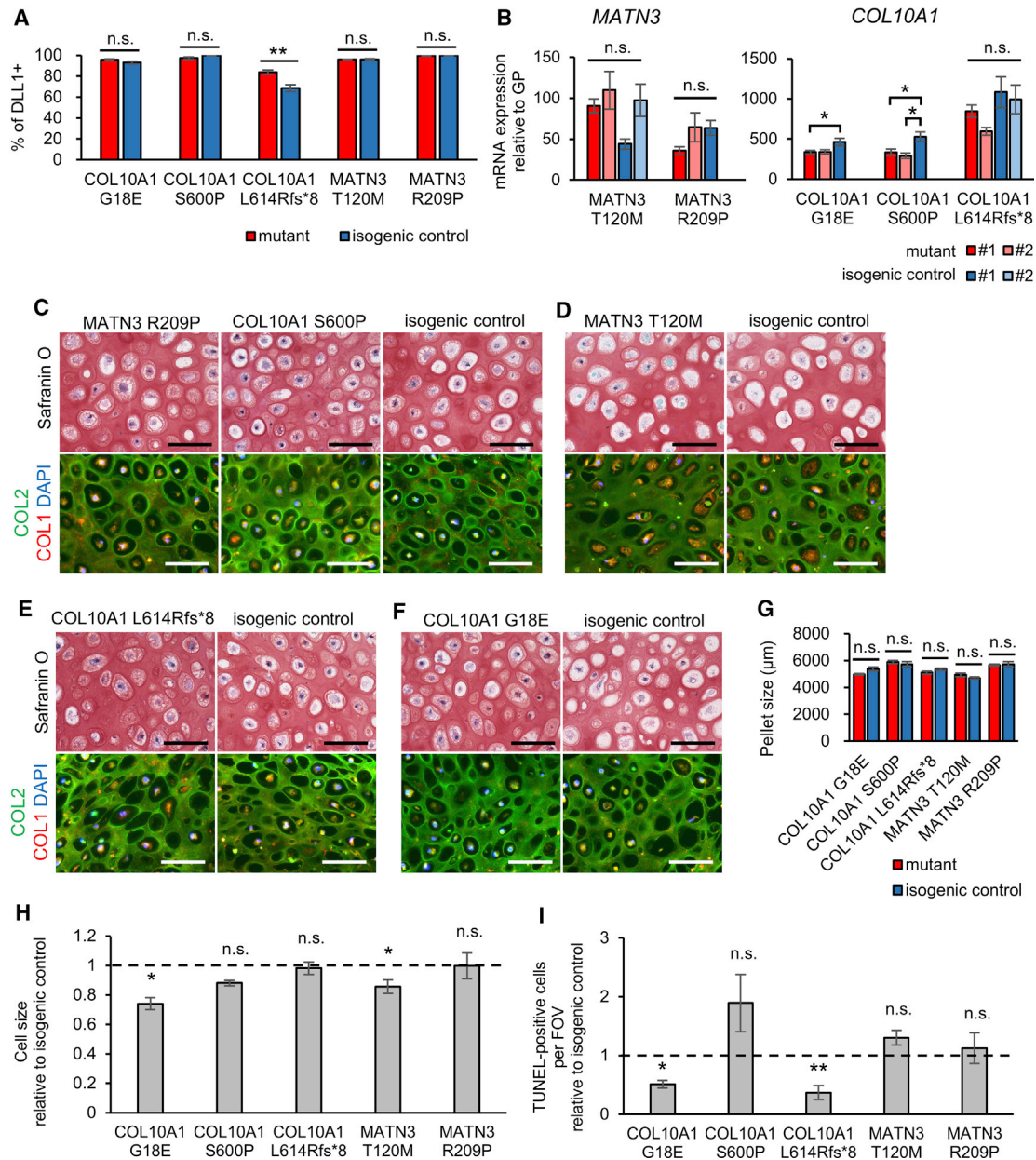


Figure 2. COL10A1 and MATN3 mutants show no disruption of chondrogenic differentiation

(A) Percentage of DLL1-positive cells on day 2 of SI.

(B) mRNA expression of the heterozygously mutated gene by qPCR, with values from a second clone also shown for each mutant and isogenic control (number of independent experiments shown in Table S2). Values are relative to the mean of six pieces of the human distal femoral growth plate. Statistical analysis by ANOVA and post hoc Tukey's HSD.

(C–F) Safranin O staining (top panels) or COL2 (green) and COL1 (red) immunostaining (bottom panels) of mutants (left panels) and their isogenic controls (right panels). Similar results were obtained in $n = 4$ independent experiments. Scale bars, 100 µm.

(G) Pellet size of each mutant and its isogenic control. Three technical replicates per independent experiment were measured.

(H) Cell size of each mutant relative to the isogenic control, quantified from the inverse image of COL2 fluorescence.

(I) TUNEL-positive cells per FOV (field of view) relative to the isogenic control of each mutant.

All results except (A) are from day 56 of HI. Values are expressed as mean \pm SEM. Dotted lines indicate the value = 1 of the isogenic controls in (H) and (I). Except where stated otherwise, the results are from $n = 4$ independent experiments, and statistical analysis was performed using unpaired two-sided t tests. (n.s., no significant difference; $*p < 0.05$, $**p < 0.01$). See also Figures S2–S5.

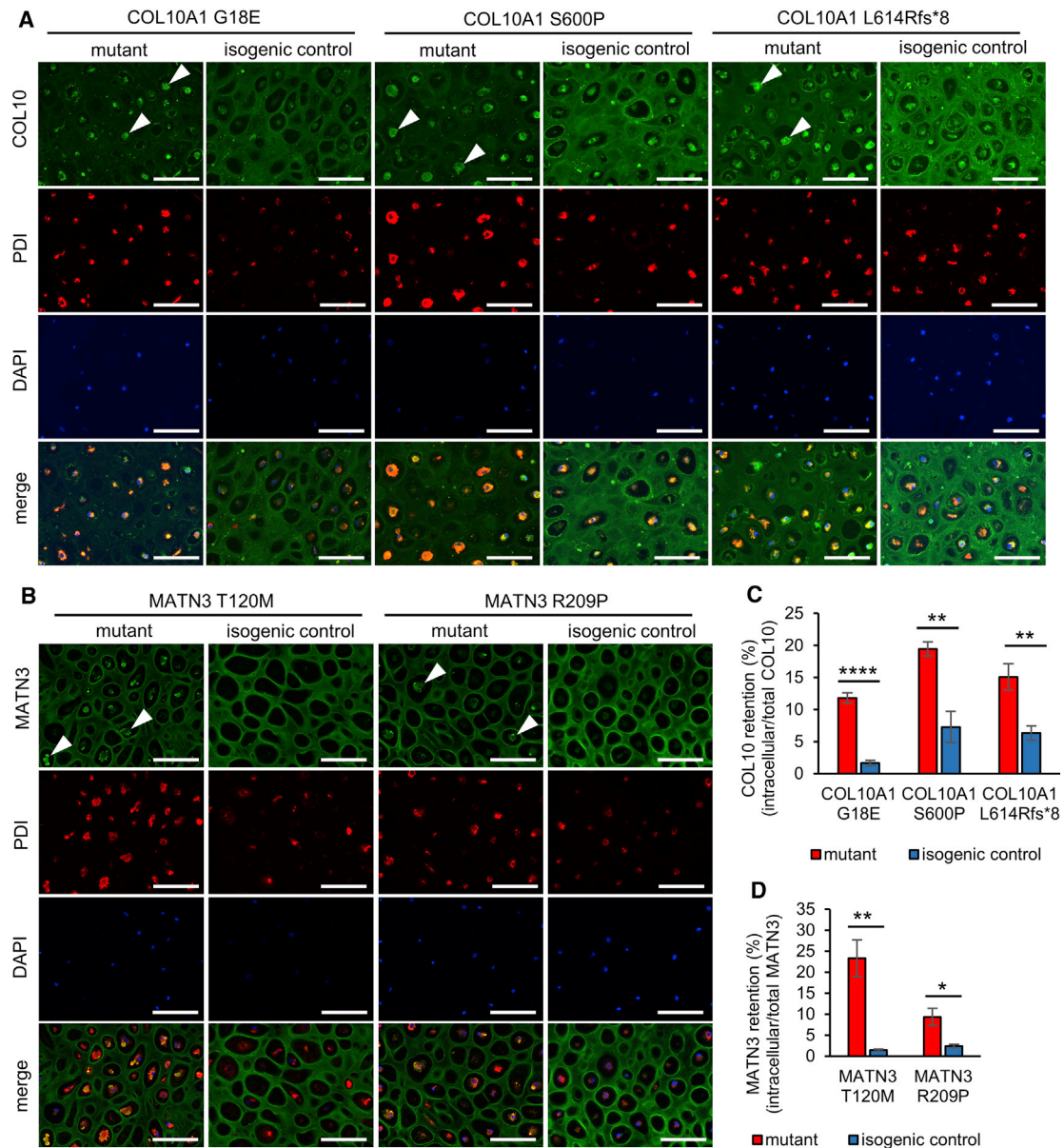


Figure 3. COL10A1 and MATN3 mutants retain COL10 or MATN3 within the ER

(A and B) Immunostaining of COL10 (A) or MATN3 (B) and PDI on day 56 of HI. Arrowheads indicate intracellular aggregates in mutants. Similar results were obtained in $n = 4$ independent experiments. Scale bars, 100 μm .

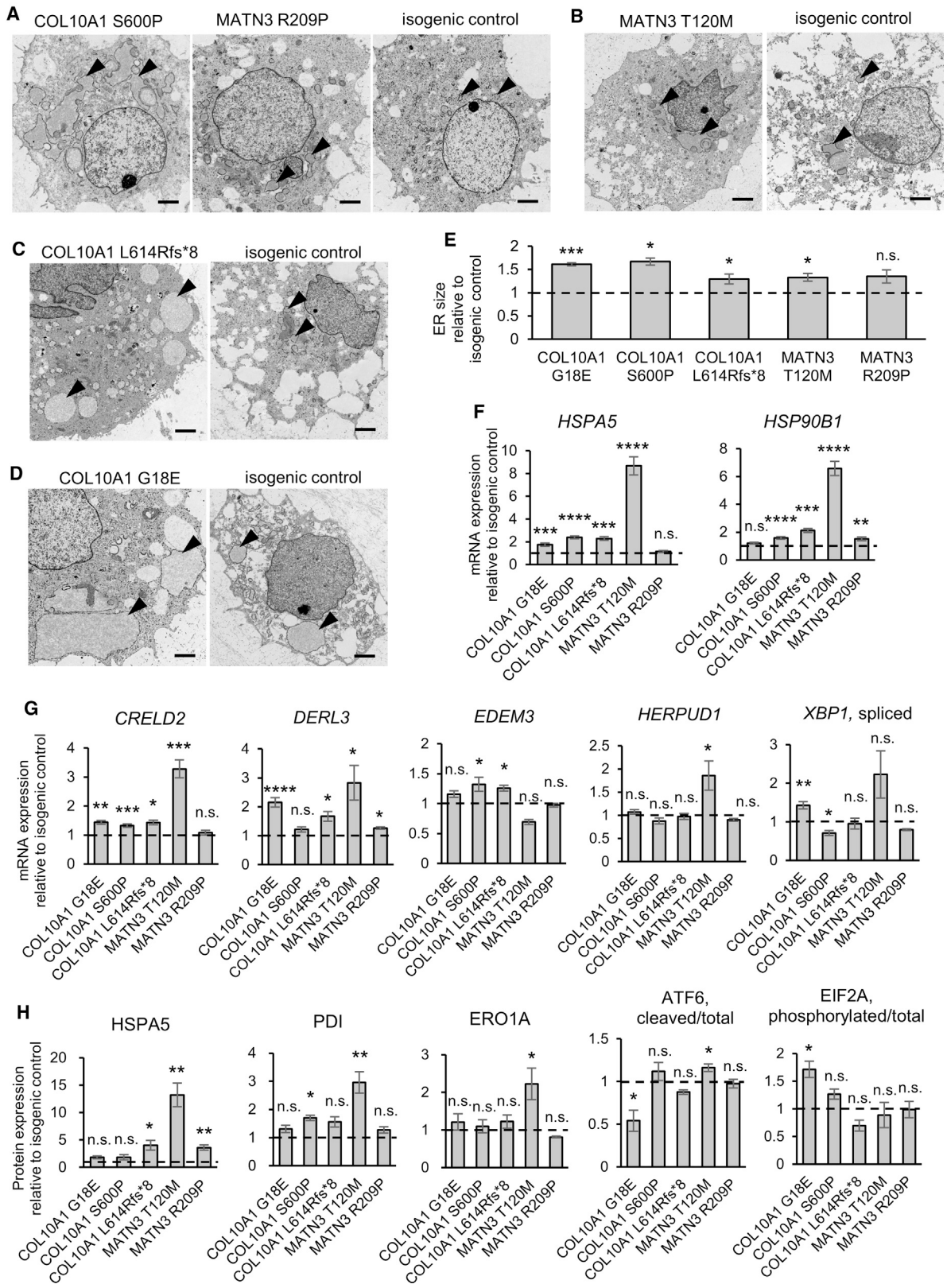
(C and D) Intracellular retention quantified from fluorescence intensity of COL10 (C) or MATN3 (D) co-staining with PDI (intracellular) divided by total fluorescence intensity in $n = 4$ independent experiments on day 56 of HI. Values are expressed as mean \pm SEM. (n.s., no significant difference; * $p < 0.05$, ** $p < 0.01$, **** $p < 0.0001$ by unpaired two-sided t test).

See also Figure S5.

ER expansion, ER stress, and a UPR are detected in some but not all mutants

To analyze the impact of intracellular COL10 or MATN3 accumulation in human cartilage, we next used transmission electron microscopy to assess the ER, which was found to be mildly to severely enlarged in mutants (Figures 4A–

4D). Quantification of the PDI-positive areas confirmed these results, with all but the MATN3 R209P mutant showing a significant increase in ER size (Figure 4E). We next examined ER stress and UPR markers at the mRNA and protein level, revealing significant increases in one or more markers in every mutant (Figures 4F–4H and SSE).



(legend on next page)



The largest changes were seen in the MATN3 T120M mutant, which showed high expression of the chaperones HSPA5, HSP90B1, and PDI, as well as increased ATF6 cleavage and upregulation of downstream UPR genes CRELD2, DERL3, HERPUD1, and ERO1A. Activation of the ATF6 branch was also reported in MATN3 V194D model mice (Pirog et al., 2019), but this was not observed in our MATN3 R209P mutant, which had little to no increase in ER stress and UPR markers. In the case of COL10A1 mutants, COL10A1 G18E showed an increase in spliced XBP1 and phosphorylated EIF2A, as well as greater expression of CRELD2 and DERL3, suggesting the activation of PERK and IRE1 branches. COL10A1 N617K model mice have also shown IRE1 and PERK activation (Cameron et al., 2011), but the activation of these branches was not clear in our COL10A1 S600P and L614Rfs*8 mutants.

Zonal disorganization in growth-plate-like structures

Since cell morphology and chondrocyte maturation markers in mutants showed little or no change in our *in vitro* system, we next assessed whether an *in vivo* environment may allow the detection of further differences. iPSC-derived sclerotome cells, which served as the chondroprogenitors in our *in vitro* model, were transplanted into immunodeficient mice to allow spontaneous development into tissues including cartilage and self-organizing growth-plate-like structures (previously described in Matsuda et al., 2020 and Loh et al., 2016). Histological examination of the tissues 56 days after transplantation revealed growth-plate-like structures both in mutants and isogenic controls, with similar Safranin O and von Kossa staining (Figures 5A and 5B).

However, in the COL10A1 G18E mutant, chondrocyte morphology changed little throughout the structure, and no distinct zonal accumulation of hypertrophic chondrocytes could be observed ahead of the mineralized areas, reflecting the morphological changes in hypertrophic chondrocytes to a smaller, more proliferating chondrocyte-like morphology observed in mouse models (Rajpar et al., 2009). In the MATN3 T120M mutant, cells with a hypertrophic morphology were observed throughout the growth-plate-like structure, which lacked columnar chondrocytes

similarly to mouse models (Leighton et al., 2007). In both mutants, COL2 and COL1 production was unaffected, confirming the results of the *in vitro* observations, while COL10 expression was variable (Figures 5C and 5D). Ki67 mostly stained in areas where cells had a proliferating chondrocyte-like morphology, while TUNEL staining was mostly observed in the hypertrophic-like areas, without a notable increase. HSPA5 stained weakly in both the COL10A1 G18E mutant and isogenic control, but more intensely in the MATN3 T120M mutant compared with the isogenic control, confirming the severe ER stress of the latter observed *in vitro*.

To examine whether COL10A1 and MATN3 mutations affect the amount of mineralization, we transplanted cartilage pellets created using our *in vitro* system into immunodeficient mice on day 28 of HI. Within 20 days, mineralization was detected in all mutants and isogenic controls (Figure 5E), but the area of mineralization was not different between the isogenic pairs (Figure 5F).

Application of the *in vitro* model to transcriptomics and drug testing

Due to the differences in ER stress levels and UPR activation in each mutant, we next asked whether our *in vitro* model could be used to further examine the effects of each MATN3 and COL10A1 mutation on the transcriptome. Microarray analysis revealed large differences in the amount of differentially expressed genes (DEGs) in each mutant. The COL10A1 G18E, COL10A1 L614Rfs*8, and MATN3 R209P mutants showed only few DEGs with false discovery rate (FDR)-adjusted p value of <0.05, suggesting that these mutations are mostly tolerated *in vitro* (Figure 6A). However, the COL10A1 S600P and MATN3 T120M mutations led to wide-ranging changes in multiple signaling pathways and cellular functions (Figures 6B, 6C, and S6A–S6D; Table S1).

For both mutants, top terms in the IPA Tissue Development category were related to bone size, thickness, and morphology, exemplified by the common upregulation of CXXC5, GPNMB, and CHAD, known to be involved in bone homeostasis and osteoblast differentiation (Figure 6B) (Frara et al., 2016; Hesse et al., 2013; Kim et al., 2015).

Figure 4. Some, but not all, COL10A1 and MATN3 mutants show an increased ER size, ER stress, and a UPR

(A–D) Transmission electron microscopy of mutants (left panels) and their isogenic controls (right panels). Arrowheads indicate the ER. Scale bars, 2 μ m.

(E) ER size quantified from the area of PDI fluorescence from n = 4 independent experiments.

(F and G) mRNA expression of ER stress markers (F) and UPR markers (G) by qPCR (number of independent experiments shown in Table S2).

(H) Protein expression of ER stress and UPR markers by Simple Western (HSPA5, PDI, ERO1A) or western blotting (ATF6, EIF2A) from n = 4 independent experiments.

All results are from day 56 of HI and are expressed as mean \pm SEM, relative to the respective isogenic control (dotted lines). Statistical analysis was performed by unpaired two-sided t test (n.s., no significant difference; *p < 0.05, **p < 0.01, ***p < 0.001, ****p < 0.0001). See also Figure S5.

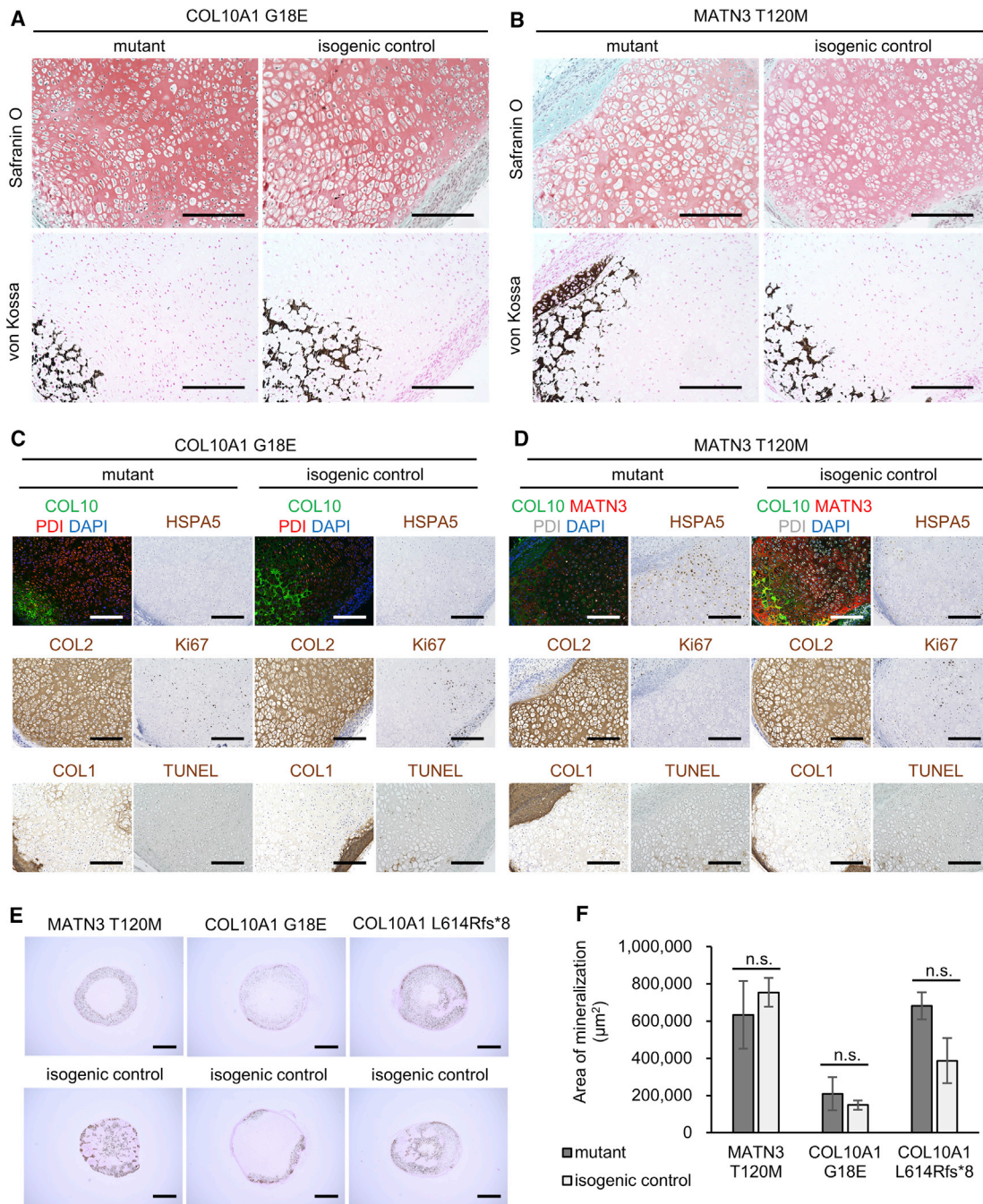


Figure 5. COL10A1 and MATN3 mutants show zonal disorganization without change in mineralization

(A and B) Histology of growth-plate-like structures from tissue collected on day 56 after transplantation into immunodeficient mice. (Top) Safranin O staining; (bottom) von Kossa staining. Similar results were observed in two or more growth-plate-like structures for each clone. Scale bars, 200 μm.

(C and D) Immunofluorescence, immunohistochemistry, and TUNEL staining of the growth-plate-like structures in (A) and (B). Scale bars, 200 μm.

(E) von Kossa staining of mutant (top) or isogenic control (bottom) pellets transplanted on day 28 of HI and collected after 20 days *in vivo*. Similar results were obtained in six pellets transplanted into three different mice (two pellets per mouse). Scale bars, 1 mm.

(F) Quantification of von Kossa-positive areas. Values are expressed as mean ± SEM. Results are calculated as n = 3 from three different mice with two pellets each. (n.s., no significant difference by unpaired two-sided t test).

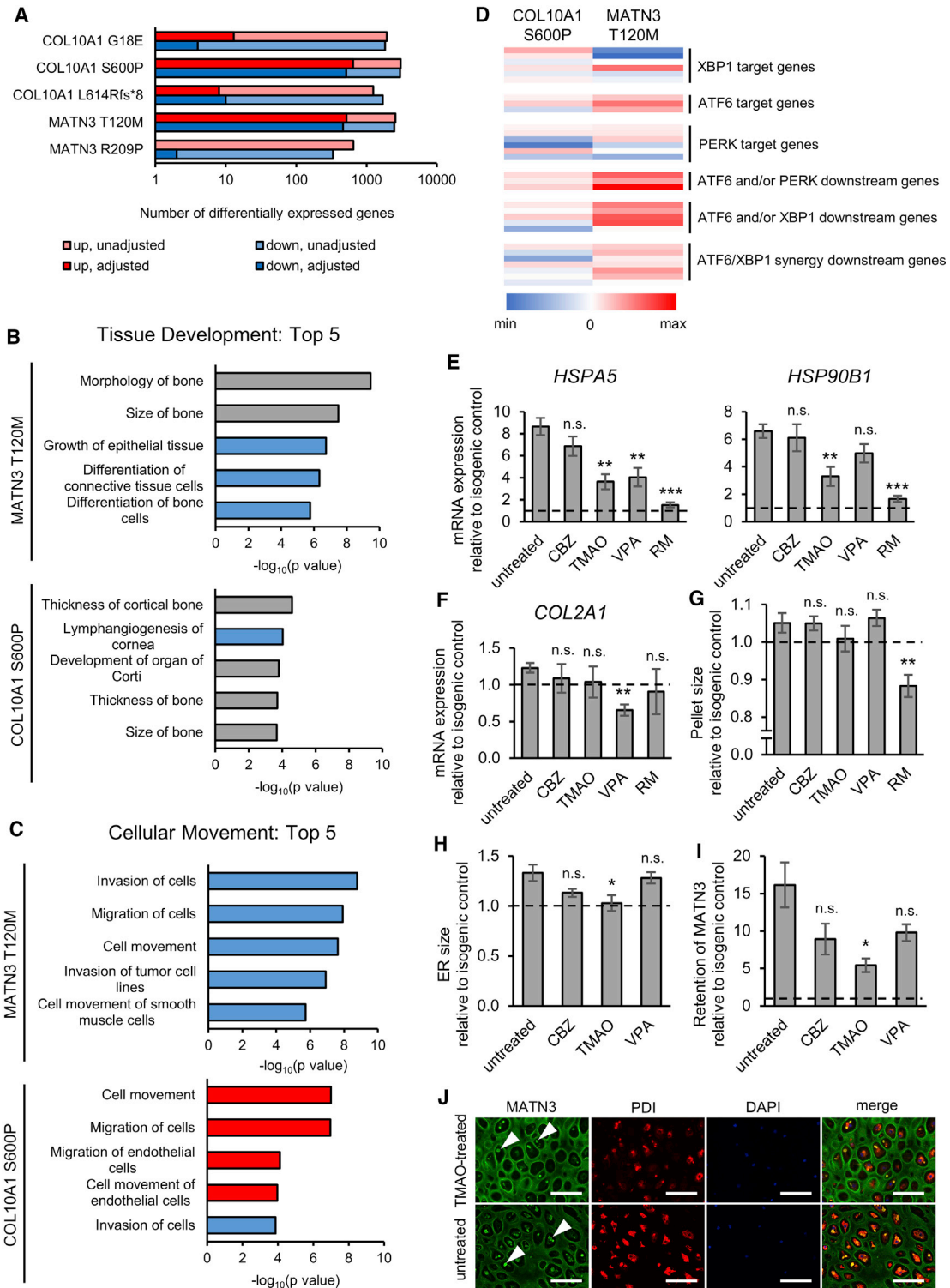


Figure 6. iPSC-derived hypertrophic chondrocytes allow drug testing and further exploration of chondrodysplasia pathology

(A) Number of differentially expressed genes by microarray analysis using FDR-adjusted or unadjusted p value of <0.05 by moderated t test in each mutant compared with its isogenic control.

(B and C) Top five Tissue Development (B) and Cellular Movement (C) terms in IPA Diseases and Functions for the MATN3 T120M and COL10A1 S600P mutants versus their isogenic controls by microarray analysis. Genes with adjusted p value of <0.05 by moderated t test (legend continued on next page)



However, while both mutants showed changes in the Cellular Movement category, many were in the opposite direction (Figure 6C). In the COL10A1 S600P mutant, the integrins *ITGA8*, *ITGA11*, *ITGB2*, and *ITGB3* were downregulated, with ILK and integrin signaling among the most significantly affected pathways (Figure S6B). The MATN3 T120M mutant had significant changes in several extracellular matrix (ECM) proteins, with decreased *TNC*, *LAMA4*, and *POSTN*, and increased *COMP* expression. Interestingly, both mutants showed a negative change in angiogenesis-related terms in the Organismal Development category, with a common downregulation of *VEGFC* and an upregulation of thrombospondins *THBS2* or *THBS3* in the COL10A1 S600P and MATN3 T120M mutants, respectively (Figure S6C). In the Small Molecule Biochemistry category, MATN3 T120M led to upregulated sterol synthesis through increases in *INSIG1*, *SQLE*, *HMGCR*, and *SREBF2*, while the changes in the COL10A1 S600P mutant included amino acid uptake and glucose metabolism (Figure S6D).

Together, these results indicate that these mutations result in both common and unique changes in cell-matrix interactions, metabolism, matrix composition, and bone homeostasis that can be detected using our system. This is despite the weaker ER stress and the unclear UPR activation in the COL10A1 S600P mutant, which had increases in the ER stress response genes *CREB3*, *SERP1*, and *CRYAB*, but in only few of the canonical UPR genes (Figure 6D, details in Table S1). In the MATN3 T120M mutant, however, the UPR was one of the most significantly affected pathways, mostly through the activation of ATF6 target and downstream genes that have been reported in the MATN3 V194D model mice (Pirog et al., 2019) (Figures S6A and 6D).

Therefore, we next utilized the MATN3 T120M mutant to examine the possibility of our system to be used as a drug-testing platform. As autophagy inducers and chemical

chaperones have been shown to improve the phenotype in models of skeletal dysplasias (Forouhan et al., 2018; Kawai et al., 2019; Okada et al., 2015; Posey et al., 2014), we assessed their effect on this mutant on day 56 of HI after 28 days of treatment. Both *HSPA5* and *HSP90B1* were significantly reduced using trimethylamine N-oxide (TMAO) and rapamycin (RM), neither of which affected *COL2A1* expression, but RM led to a significant reduction of pellet size, indicating a possible disruption of ECM production (Figures 6E–6G). TMAO was also successful in reducing the ER size and intracellular MATN3 retention in this mutant, demonstrating a marked alleviation of its phenotype in our system (Figures 6H–6J).

DISCUSSION

In this study, we developed a robust, serum-free protocol to induce hypertrophic chondrocytes from iPSCs to model chondrodysplasias in a 3D culture system. This protocol mimics the process of chondrocyte differentiation in the growth plate, with cells characteristic of hypertrophic chondrocytes in their morphology as well as their gene expression being obtained after 56 days in 3D culture. Genes that are highly upregulated in the physis but not articular cartilage, such as *MATN3* and *COL9A2* (Paradise et al., 2018), were expressed in the course of induction, supporting the validity of our model to research disorders of the growth plate.

Using this system, we found that *MATN3* and *COL10A1* mutants had intracellular accumulation of the affected protein and an increased expression of ER stress markers, the severity of which depended on the mutation. Strong activation of UPR genes was detected only in the MATN3 T120M mutant, indicating heterogeneity in the phenotype even when mutations are in the same disease-causing gene.

were used for IPA. Red bars, positive activation Z score; blue bars, negative activation Z score; gray bars, zero or unavailable activation Z score.

(D) Heatmap of the log₂ fold change of UPR genes from different branches in the COL10A1 S600P and MATN3 T120M mutants by microarray analysis.

(E and F) mRNA expression of ER stress markers (E) and chondrocyte marker *COL2A1* (F) by qPCR in the MATN3 T120M mutant with and without drug treatment.

(G) Pellet size of the MATN3 T120M mutant with and without treatment.

(H) ER size of the MATN3 T120M mutant with and without treatment, quantified from the area of PDI fluorescence.

(I) Intracellular retention of MATN3 in the MATN3 T120M mutant with and without treatment, quantified from fluorescence intensity of MATN3 co-staining with PDI (intracellular) divided by total fluorescence intensity.

(J) Immunostaining of MATN3 and PDI in the MATN3 T120M mutant with and without treatment. Arrowheads indicate intracellular aggregates. Similar results were obtained in n = 4 independent experiments. Scale bars, 100 μm.

All results are from day 56 of HI. The number of independent experiments is n = 3 in (A) to (D) and n = 4 in (E) to (I). In (E) to (I), values are expressed as mean ± SEM, relative to the isogenic control (dotted lines), and statistical analysis was performed by unpaired two-sided t test of treated compared with untreated samples (n.s., no significant difference; *p < 0.05, **p < 0.01, ***p < 0.001). As experiments were performed at the same time, data of untreated mutants and isogenic controls in (E) to (J) are the same as in Figures 2G, 3D, 4E, 4F, and S5A. CBZ, carbamazepine; TMAO, trimethylamine N-oxide; VPA, valproic acid; RM, rapamycin. See also Figure S6 and Table S1.



The patient with the *MATN3* T120M mutation had a short stature (−2.2 SD) and a severe phenotype in the radiological findings, with skeletal abnormalities reminiscent of spondyloepimetaphyseal dysplasia, matrilin 3 type (SEMD-MATN3; OMIM #608728), which is caused by homozygous *MATN3* mutations (Borochowitz et al., 2004). Since the SNP rs187943382, causing *MATN3* V220A, was found in the healthy allele of *MATN3* in this patient, we cannot exclude that it could exacerbate the pathology caused by T120M, as both are within the von Willebrand factor type A (vWFa) domain and may act in synergy to worsen the misfolding. Because V220A has also been detected in healthy controls (Kim et al., 2011), and the rescue of the *MATN3* T120M mutant showed no intracellular accumulation of *MATN3*, we propose that this SNP may only worsen existing MED pathology without causing it on its own. In contrast to the *MATN3* T120M mutant, the *MATN3* R209P mutant had only few transcriptomic changes and little ER stress. The height of the R209P patient was in the 51st percentile (Kim et al., 2011), indicating that this mutation may result in fewer structural changes in *MATN3* and a milder phenotype than other mutations, which caused very short statures. These observations indicate that our system is capable of recapitulating the differences in phenotype severity of MED patients with mutations in *MATN3*.

However, the genotype-phenotype relationship in the *COL10A1* mutants was less clear. Despite the different types and locations of the mutations in *COL10A1*, the MCDS patients all had a similar phenotype typical of this chondrodysplasia. One of the patients had a previously unreported *COL10A1* L614Rfs*8 frameshift mutation in the NC1 domain, which did not lead to NMD despite the early stop codon. This suggests that unlike the Y632X mutation (Chan et al., 1998), this mutation will not result in haploinsufficiency and likely acts in a gain-of-function manner similar to that of substitution mutations in the same domain. The *COL10A1* G18E mutation, however, likely leads to impaired signal peptide cleavage and failure to release the *COL10A1* chains into the ER lumen (Chan et al., 2001). Our results also show an enlargement of the ER and a mild increase of UPR markers in this mutant, possibly causing a phenotype with similar molecular mechanisms to mutations in the NC1 domain. Nevertheless, neither L614Rfs*8 nor G18E led to substantial changes in the transcriptome, raising the possibility that their phenotype was not completely recapitulated in our system or may require environmental factors such as mechanical stresses to fully manifest.

Indeed, in both *MATN3* and *COL10A1* mutants, changes in chondrocyte maturation markers were small, and changes in cell morphology required an *in vivo* environment to appear. Together with the expression of *COL2A1*

remaining high on day 56, this suggests that our *in vitro* system may still lack some of the required regulatory network. However, a distinct advantage of our *in vitro* model over the *in vivo* sclerotome transplantation is the stability of results across different iPSC lines, allowing for the quantification and detection of mild changes as well as drug testing. In contrast, the formation of *in vivo* growth-plate-like structures was rare and spontaneous, with the variability in their size and orientation precluding the quantification of the length of the proliferating and hypertrophic zones, the latter of which has been reported to extend in *Col10a1* mutant mice (Rajpar et al., 2009). Therefore, improving on the stability of the *in vivo* model or developing an *in vitro* model that includes both proliferating and hypertrophic chondrocytes in separate zones, similarly to a growth plate *in vivo*, may greatly expand the capabilities of chondrodysplasia-specific iPSCs to precisely recapitulate the disease phenotype.

Despite these limitations, the *MATN3* T120M and *COL10A1* S600P mutants displayed wide-ranging transcriptomic changes in our *in vitro* model. Since the *COL10A1* S600P mutant, contrary to mouse models of MCDS (Wang et al., 2018), showed almost no signs of activation of any of the UPR branches, this raises the question of whether the UPR is always a key disease mechanism of MCDS in humans. *COL10A1* N617K model mice had little to no phenotype when heterozygous (Rajpar et al., 2009), and while *COL10A1* Y632X mutant mRNA was stable in model mice (Forouhan et al., 2018), no Y632X mutant mRNA transcripts were found in humans (Chan et al., 1998), so that species differences may exist in the exact effects of each mutation. In our *COL10A1* S600P mutant, changes in genes involved in cell-matrix signaling and bone homeostasis were detected, but the molecular mechanisms are unclear. As *CREB3*, *CREB3L1*, and the vesicular trafficking genes *ARF1*, *ARF4*, and *MIA3* were upregulated, the mild ER stress in this mutant may result in altered protein secretion and ECM composition, which may be further affected by the increase in the ECM modulators *TIMP1* and *ADAM15*. Interestingly, *ADAM15* has been found to have inhibitory effects on apoptosis in osteoarthritic chondrocytes (Böhm et al., 2010), but whether apoptosis is a disease mechanism in MCDS is unclear (Cameron et al., 2015). Since we did not observe an increase in TUNEL-positive cells *in vitro* or *in vivo*, the ER stress in the human heterozygous *COL10A1* and *MATN3* mutants is, at least at the tested time point, not strong enough to induce the apoptotic pathway and may instead trigger the adaptive response.

While there was little evidence of a canonical UPR driving the pathology in the *COL10A1* S600P mutant, many of the most significantly upregulated genes from the microarray analysis of the *MATN3* T120M mutant were related to ER stress and the UPR, including *PDIA4*,



HSP90B1, *MANF*, *HSPA5*, *HYOU1*, and *CRELD2*. Upregulation of *MANF* and *CRELD2* has also been reported in MATN3 V194D mouse and *in vitro* models due to inappropriate disulfide bond formation in mutant MATN3 (Hartley et al., 2013), suggesting that the molecular mechanism by which the T120M mutation disrupts folding may be similar. In our model, the MATN3 T120M mutant mainly activated ATF6 target and downstream genes, resulting in expression changes related to functions such as bone homeostasis and lipid metabolism, as well as ECM proteins. As cholesterol production regulates hedgehog signaling in differentiating chondrocytes (Tsushima et al., 2018), the increase of genes related to cholesterol biosynthesis and the decrease of *IHH* expression in MATN3 T120M is one possible mechanism by which cartilage maturation may be altered in this mutant, but whether these changes are pathological or adaptive remains to be established. Since the UPR is likely a key disease trigger, and treatment with the chemical chaperone TMAO was able to decrease intracellular MATN3 retention as well as ER stress markers, chaperones provide a promising therapeutic avenue for MED caused by this mutation.

Taken together, our results show that our system of hypertrophic chondrocyte differentiation from iPSCs serves as an initial platform for the study of human chondrodysplasias and drug development *in vitro*. Surprisingly mild phenotypes in MATN3 R209P, COL10A1 G18E, and COL10A1 L614Rfs*8 compared with MATN3 T120M and COL10A1 S600P mutants in our model indicate that the effects on cell behavior caused by mutations even in the same gene are highly diverse. With further improvements of our model to more completely recapitulate MED and MCDS phenotypes *in vitro*, we expect it to become a valuable tool to better assess rare patient mutations, shed light on the genotype-phenotype relationships, and perform drug screening for different chondrodysplasia mutations in the future.

EXPERIMENTAL PROCEDURES

Establishment of iPSC lines and isogenic controls

Patient iPSC lines were established from skin fibroblasts (MCDS patient #1) or peripheral blood mononuclear cells (MCDS patient #2 and MED patient) as previously described (Okita et al., 2011). Gene-corrected rescues were created using the CRISPR/Cas9 system. Further details are available in [Supplemental information](#), including guide RNAs and repair templates in [Table S3](#). All experiments with human subjects were performed with written informed consent and approved by the Ethics Committee of the Department of Medicine and Graduate School of Medicine, Kyoto University, the Ethics Committee of the Shiga Medical Center for Children, and the Ethical Committee of RIKEN Yokohama Institute.

Sclerotome and hypertrophic chondrocyte induction

All iPSCs were maintained feeder-free on dishes coated with iMatrix-511 silk (Nippi) in StemFit AK02N (Ajinomoto) with 50 U of penicillin and 50 µg/mL streptomycin (Gibco). Cells were passaged at a density of 1.1×10^3 to 3.2×10^3 cells/cm² 5 days before induction. SI was performed for 6 days as previously described, after which cells were detached and resuspended in CDMi base medium containing 100 nM SAG (Calbio), 600 nM LDN193189 (Stemgent), and 10 µM Y-27632 (Wako) (Matsuda et al., 2020). Cells were seeded into low-attachment 96-well plates (SUMILON) at 2.5×10^5 cells/well and, on the next day, i.e., day 0 of HI, induced as previously described for the first 14 days (Umeda et al., 2012). In brief, on day 0, the medium was changed to basal chondrogenic medium supplemented with 40 ng/mL PDGF-BB (R&D) and 0.1 µM dexamethasone (Wako). From day 6, 10 ng/mL TGFβ3 (R&D) was additionally supplemented. From day 10, PDGF-BB was removed and 50 ng/mL BMP4 (R&D) was added.

Then, from day 14, dexamethasone and TGFβ3 were removed, and 10 nM triiodothyronine (T3) (Sigma) was added. From day 28, 10 mM β-glycerophosphate (Sigma) was added. For the drug-treated groups, 20 µM carbamazepine (CBZ) (Sigma), 50 mM trimethylamine N-oxide (TMAO) (Sigma), 200 µM valproic acid (VPA) (Sigma), or 10 nM rapamycin (RM) (MedChem Express) was added from days 28 to 56 of HI. The CDMi and basal chondrogenic medium compositions and other information about induction are detailed in [Supplemental information](#), including key reagents in [Table S6](#). All independent experiments in this study refer to pellets from separate differentiations.

Animal experiments

For observation of growth-plate-like structures, cells were detached on day 6 of SI and resuspended in CDMi containing 100 nM SAG, 600 nM LDN193189, and 10 µM Y-27632 at a concentration of up to 1×10^8 cells/mL. This cell suspension was mixed 1:1 with Matrigel (BD) and 100 µL was injected subcutaneously into a minimum of six male immunodeficient NOD/ShiJic-scid Jcl (NOD-SCID) mice (CLEA Japan) as previously described (Matsuda et al., 2020). The transplanted tissue was collected after 56 days. For quantification of mineralization of cartilage, pellets were transplanted subcutaneously into three male NOD-SCID mice on day 28 of HI. Pellets were collected after 20 days. All animal experiments were approved by the UCSF Institutional Animal Care and Use Committee and performed in accordance with the Regulations on Animal Experimentation at Kyoto University.

Expression analysis and flow cytometry

After RNA extraction using the RNeasy Micro or Mini Kit (-QIAGEN), quantitative PCR (qPCR) was performed with the Thunderbird SYBR qPCR Mix (Toyobo). Microarray analysis was performed with the Human Gene 1.0ST Array (Affymetrix). Protein expression was analyzed by western blotting and Simple Western (ProteinSimple). Flow cytometry was performed using FACS Aria II (BD) as previously described (Matsuda et al., 2020) with minor modifications. More details are provided in [Supplemental information](#), including primer information in [Table S5](#).



Histological analysis

In vitro pellets and *in vivo* tissue were fixed in 4% paraformaldehyde for 2 days before paraffin embedding. Staining protocols are detailed in [Supplemental information](#).

Data and code availability

The microarray data are available in the GEO database under the accession numbers GEO: GSE148728 and GEO: GSE157955.

SUPPLEMENTAL INFORMATION

Supplemental information can be found online at <https://doi.org/10.1016/j.stemcr.2021.01.014>.

AUTHOR CONTRIBUTIONS

Y.P., S.K., and J.T. designed the study. Y.P. developed the HI protocol, performed the gene editing and disease modeling, analyzed all experiments, and drafted the manuscript. S.N. and M.N. assisted in the *in vitro* and *in vivo* experiments, respectively. M.W. assisted in data analysis. S.T. supervised the establishment of patient iPSC lines. C.A. and Y.Y. devised the SI and transplantation protocols. J.-Y.X. and Z.W. performed the mutation search by NGS. K.F., M.T., T.F., and S.I. provided patient samples for the establishment of iPSC lines. J.T. supervised the study and revised the manuscript, which was further reviewed by all authors.

CONFLICTS OF INTEREST

The authors declare no competing interests.

ACKNOWLEDGMENTS

We thank J. Ma and T. Nakashima for their assistance in the *in vitro* and *in vivo* experiments, respectively, H. Maekawa for providing human growth plate samples, and H. Yoshitomi, Y. Jin, and T. Takarada for comments and discussion. Preparation of tissue slides and staining was supported by the Center for Anatomical, Pathological and Forensic Medical Research, Graduate School of Medicine, Kyoto University, and Applied Medical Research Laboratory. Karyotyping was performed by Chromocenter. This study was supported by a grant-in-aid for the Acceleration Program for Intractable Disease Research Utilizing Disease Specific iPSC Cells (AMED) for S.I. and J.T. and the Centers for Clinical Application Research on Specific Disease/Organ (type B) grants (AMED) for J.T.

Received: April 30, 2020

Revised: January 23, 2021

Accepted: January 25, 2021

Published: February 25, 2021

REFERENCES

Böhm, B., Hess, S., Krause, K., Schirner, A., Ewald, W., Aigner, T., and Burkhardt, H. (2010). ADAM15 exerts an antiapoptotic effect on osteoarthritic chondrocytes via up-regulation of the X-linked inhibitor of apoptosis. *Arthritis Rheum.* *62*, 1372–1382.

Borochowitz, Z.U., Scheffer, D., Adir, V., Dagoneau, N., Munnich, A., and Cormier-Daire, V. (2004). Spondylo-epi-metaphyseal

dysplasia (SEMD) matrilin 3 type: homozygote matrilin 3 mutation in a novel form of SEMD. *J. Med. Genet.* *41*, 366–372.

Cameron, T.L., Bell, K.M., Gresshoff, I.L., Sampurno, L., Mullan, L., Ermann, J., Glimcher, L.H., Boot-Handford, R.P., and Bateman, J.F. (2015). XBP1-independent UPR pathways suppress C/EBP- β mediated chondrocyte differentiation in ER-stress related skeletal disease. *PLoS Genet.* *11*, e1005505.

Cameron, T.L., Bell, K.M., Tatarczuch, L., Mackie, E.J., Rajpar, M.H., McDermott, B.T., Boot-Handford, R.P., and Bateman, J.F. (2011). Transcriptional profiling of chondrodysplasia growth plate cartilage reveals adaptive ER-stress networks that allow survival but disrupt hypertrophy. *PLoS One* *6*, e24600.

Chan, D., Ho, M.S., and Cheah, K.S. (2001). Aberrant signal peptide cleavage of collagen X in Schmid metaphyseal chondrodysplasia. Implications for the molecular basis of the disease. *J. Biol. Chem.* *276*, 7992–7997.

Chan, D., Weng, Y.M., Graham, H.K., Sillence, D.O., and Bateman, J.F. (1998). A nonsense mutation in the carboxyl-terminal domain of type X collagen causes haploinsufficiency in schmid metaphyseal chondrodysplasia. *J. Clin. Invest.* *101*, 1490–1499.

Cotterill, S.L., Jackson, G.C., Leighton, M.P., Wagener, R., Mäkitie, O., Cole, W.G., and Briggs, M.D. (2005). Multiple epiphyseal dysplasia mutations in MATN3 cause misfolding of the A-domain and prevent secretion of mutant matrilin-3. *Hum. Mutat.* *26*, 557–565.

Czarny-Ratajczak, M., Lohiniva, J., Rogala, P., Kozłowski, K., Perälä, M., Carter, L., Spector, T.D., Kolodziej, L., Seppänen, U., Glazar, R., et al. (2001). A mutation in COL9A1 causes multiple epiphyseal dysplasia: further evidence for locus heterogeneity. *Am. J. Hum. Genet.* *69*, 969–980.

Forouhan, M., Sonntag, S., and Boot-Handford, R.P. (2018). Carbamazepine reduces disease severity in a mouse model of metaphyseal chondrodysplasia type Schmid caused by a premature stop codon (Y632X) in the Col10a1 gene. *Hum. Mol. Genet.* *27*, 3840–3853.

Frara, N., Abdelmagid, S.M., Sondag, G.R., Moussa, F.M., Yingling, V.R., Owen, T.A., Popoff, S.N., Barbe, M.F., and Safadi, F.F. (2016). Transgenic expression of osteoactivin/gpnb enhances bone formation *in vivo* and osteoprogenitor differentiation *ex vivo*. *J. Cell. Physiol.* *231*, 72–83.

Gregory, C.A., Zabel, B., Grant, M.E., Boot-Handford, R.P., and Wallis, G.A. (2000). Equal expression of type X collagen mRNA from mutant and wild type COL10A1 alleles in growth plate cartilage from a patient with metaphyseal chondrodysplasia type Schmid. *J. Med. Genet.* *37*, 627–629.

Hartley, C.L., Edwards, S., Mullan, L., Bell, P.A., Fresquet, M., Boot-Handford, R.P., and Briggs, M.D. (2013). Armet/Manf and Creld2 are components of a specialized ER stress response provoked by inappropriate formation of disulphide bonds: implications for genetic skeletal diseases. *Hum. Mol. Genet.* *22*, S262–S275.

Hessle, L., Stordalen, G.A., Wenglén, C., Petzold, C., Tanner, K.E., Brorson, S.H., Baekkevold, E.S., Önerfjord, P., Reinholt, F.P., and Heinegård, D. (2013). The skeletal phenotype of chondroadherin deficient mice. *PLoS One* *8*, e63080.



- Ikegawa, S., Nakamura, K., Nagano, A., Haga, N., and Nakamura, Y. (1997). Mutations in the N-terminal globular domain of the type X collagen gene (COL10A1) in patients with Schmid metaphyseal chondrodysplasia. *Hum. Mutat.* *9*, 131–135.
- Jackson, G.C., Barker, F.S., Jakkula, E., Czarny-Ratajczak, M., Mäkitie, O., Cole, W.G., Wright, M.J., Smithson, S.F., Suri, M., Rogala, P., et al. (2004). Missense mutations in the beta strands of the single A-domain of matrilin-3 result in multiple epiphyseal dysplasia. *J. Med. Genet.* *41*, 52–59.
- Karl, A., Olbrich, N., Pfeifer, C., Berner, A., Zellner, J., Kujat, R., Angele, P., Nerlich, M., and Mueller, M.B. (2014). Thyroid hormone-induced hypertrophy in mesenchymal stem cell chondrogenesis is mediated by bone morphogenetic protein-4. *Tissue Eng. Part A* *20*, 178–188.
- Kawai, S., Yoshitomi, H., Sunaga, J., Alev, C., Nagata, S., Nishio, M., Hada, M., Koyama, Y., Uemura, M., Sekiguchi, K., et al. (2019). In vitro bone-like nodules generated from patient-derived iPSCs recapitulate pathological bone phenotypes. *Nat. Biomed. Eng.* *3*, 558–570.
- Kim, H.Y., Yoon, J.Y., Yun, J.H., Cho, K.W., Lee, S.H., Rhee, Y.M., Jung, H.S., Lim, H.J., Lee, H., Choi, J., et al. (2015). CXXC5 is a negative-feedback regulator of the Wnt/ β -catenin pathway involved in osteoblast differentiation. *Cell Death Differ.* *22*, 912–920.
- Kim, O.H., Park, H., Seong, M.W., Cho, T.J., Nishimura, G., Superti-Furga, A., Unger, S., Ikegawa, S., Choi, I.H., Song, H.R., et al. (2011). Revisit of multiple epiphyseal dysplasia: ethnic difference in genotypes and comparison of radiographic features linked to the COMP and MATN3 genes. *Am. J. Med. Genet. A* *155A*, 2669–2680.
- Kobayashi, T., Chung, U.I., Schipani, E., Starbuck, M., Karsenty, G., Katagiri, T., Goad, D.L., Lanske, B., and Kronenberg, H.M. (2002). PTHrP and Indian hedgehog control differentiation of growth plate chondrocytes at multiple steps. *Development* *129*, 2977–2986.
- Kwan, K.M., Pang, M.K., Zhou, S., Cowan, S.K., Kong, R.Y., Pfordte, T., Olsen, B.R., Sillence, D.O., Tam, P.P., and Cheah, K.S. (1997). Abnormal compartmentalization of cartilage matrix components in mice lacking collagen X: implications for function. *J. Cell Biol.* *136*, 459–471.
- Leighton, M.P., Nundlall, S., Starborg, T., Meadows, R.S., Suleman, F., Knowles, L., Wagener, R., Thornton, D.J., Kadler, K.E., Boot-Handford, R.P., et al. (2007). Decreased chondrocyte proliferation and dysregulated apoptosis in the cartilage growth plate are key features of a murine model of epiphyseal dysplasia caused by a matn3 mutation. *Hum. Mol. Genet.* *16*, 1728–1741.
- Loh, K.M., Chen, A., Koh, P.W., Deng, T.Z., Sinha, R., Tsai, J.M., Barkal, A.A., Shen, K.Y., Jain, R., Morganti, R.M., et al. (2016). Mapping the pairwise choices leading from pluripotency to human bone, heart, and other mesoderm cell types. *Cell* *166*, 451–467.
- Mäkitie, O., Susic, M., Ward, L., Barclay, C., Glorieux, F.H., and Cole, W.G. (2005). Schmid type of metaphyseal chondrodysplasia and COL10A1 mutations—findings in 10 patients. *Am. J. Med. Genet. A* *137A*, 241–248.
- Matsuda, M., Yamanaka, Y., Uemura, M., Osawa, M., Saito, M.K., Nagahashi, A., Nishio, M., Guo, L., Ikegawa, S., Sakurai, S., et al. (2020). Recapitulating the human segmentation clock with pluripotent stem cells. *Nature* *580*, 124–129.
- Mortier, G.R., Cohn, D.H., Cormier-Daire, V., Hall, C., Krakow, D., Mundlos, S., Nishimura, G., Robertson, S., Sangiorgi, L., Savarirayan, R., et al. (2019). Nosology and classification of genetic skeletal disorders: 2019 revision. *Am. J. Med. Genet. A* *179*, 2393–2419.
- Mueller, M.B., and Tuan, R.S. (2008). Functional characterization of hypertrophy in chondrogenesis of human mesenchymal stem cells. *Arthritis Rheum.* *58*, 1377–1388.
- Nakagawa, M., Taniguchi, Y., Senda, S., Takizawa, N., Ichisaka, T., Asano, K., Morizane, A., Doi, D., Takahashi, J., Nishizawa, M., et al. (2014). A novel efficient feeder-free culture system for the derivation of human induced pluripotent stem cells. *Sci. Rep.* *4*, 3594.
- Okada, M., Ikegawa, S., Morioka, M., Yamashita, A., Saito, A., Sawai, H., Murotsuki, J., Ohashi, H., Okamoto, T., Nishimura, G., et al. (2015). Modeling type II collagenopathy skeletal dysplasia by directed conversion and induced pluripotent stem cells. *Hum. Mol. Genet.* *24*, 299–313.
- Okita, K., Matsumura, Y., Sato, Y., Okada, A., Morizane, A., Okamoto, S., Hong, H., Nakagawa, M., Tanabe, K., Tezuka, K., et al. (2011). A more efficient method to generate integration-free human iPSC cells. *Nat. Methods* *8*, 409–412.
- Paradise, C.R., Galeano-Garces, C., Galeano-Garces, D., Dudakov, A., Milbrandt, T.A., Saris, D.B.F., Krych, A.J., Karperien, M., Ferguson, G.B., Evseenko, D., et al. (2018). Molecular characterization of physis tissue by RNA sequencing. *Gene* *668*, 87–96.
- Pirog, K.A., Dennis, E.P., Hartley, C.L., Jackson, R.M., Soul, J., Schwartz, J.M., Bateman, J.F., Boot-Handford, R.P., and Briggs, M.D. (2019). XBP1 signalling is essential for alleviating mutant protein aggregation in ER-stress related skeletal disease. *PLoS Genet.* *15*, e1008215.
- Posey, K.L., Coustry, F., Veerisetty, A.C., Liu, P., Alcorn, J.L., and Hecht, J.T. (2014). Chondrocyte-specific pathology during skeletal growth and therapeutics in a murine model of pseudoachondroplasia. *J. Bone Miner. Res.* *29*, 1258–1268.
- Rajpar, M.H., McDermott, B., Kung, L., Eardley, R., Knowles, L., Heeran, M., Thornton, D.J., Wilson, R., Bateman, J.F., Poulosom, R., et al. (2009). Targeted induction of endoplasmic reticulum stress induces cartilage pathology. *PLoS Genet.* *5*, e1000691.
- Tsushima, H., Tang, Y.J., Puvindran, V., Hsu, S.C., Nadesan, P., Yu, C., Zhang, H., Mirando, A.J., Hilton, M.J., and Alman, B.A. (2018). Intracellular biosynthesis of lipids and cholesterol by Scap and Insig in mesenchymal cells regulates long bone growth and chondrocyte homeostasis. *Development* *145*, dev162396.
- Umeda, K., Zhao, J., Simmons, P., Stanley, E., Elefanty, A., and Nakayama, N. (2012). Human chondrogenic paraxial mesoderm, directed specification and prospective isolation from pluripotent stem cells. *Sci. Rep.* *2*, 455.
- van der Weyden, L., Wei, L., Luo, J., Yang, X., Birk, D.E., Adams, D.J., Bradley, A., and Chen, Q. (2006). Functional knockout of the matrilin-3 gene causes premature chondrocyte maturation to



hypertrophy and increases bone mineral density and osteoarthritis. *Am. J. Pathol.* *169*, 515–527.

Wang, C., Tan, Z., Niu, B., Tsang, K.Y., Tai, A., Chan, W.C.W., Lo, R.L.K., Leung, K.K.H., Dung, N.W.F., Itoh, N., et al. (2018). Inhibiting the integrated stress response pathway prevents aberrant chondrocyte differentiation thereby alleviating chondrodysplasia. *eLife* *7*, e37673.

Wang, J., Zhou, J., and Bondy, C.A. (1999). Igf1 promotes longitudinal bone growth by insulin-like actions augmenting chondrocyte hypertrophy. *FASEB J.* *13*, 1985–1990.

Wilson, R., Freddi, S., Chan, D., Cheah, K.S., and Bateman, J.F. (2005). Misfolding of collagen X chains harboring Schmid metaphyseal chondrodysplasia mutations results in aberrant disulfide bond formation, intracellular retention, and activation of the unfolded protein response. *J. Biol. Chem.* *280*, 15544–15552.

Stem Cell Reports, Volume 16

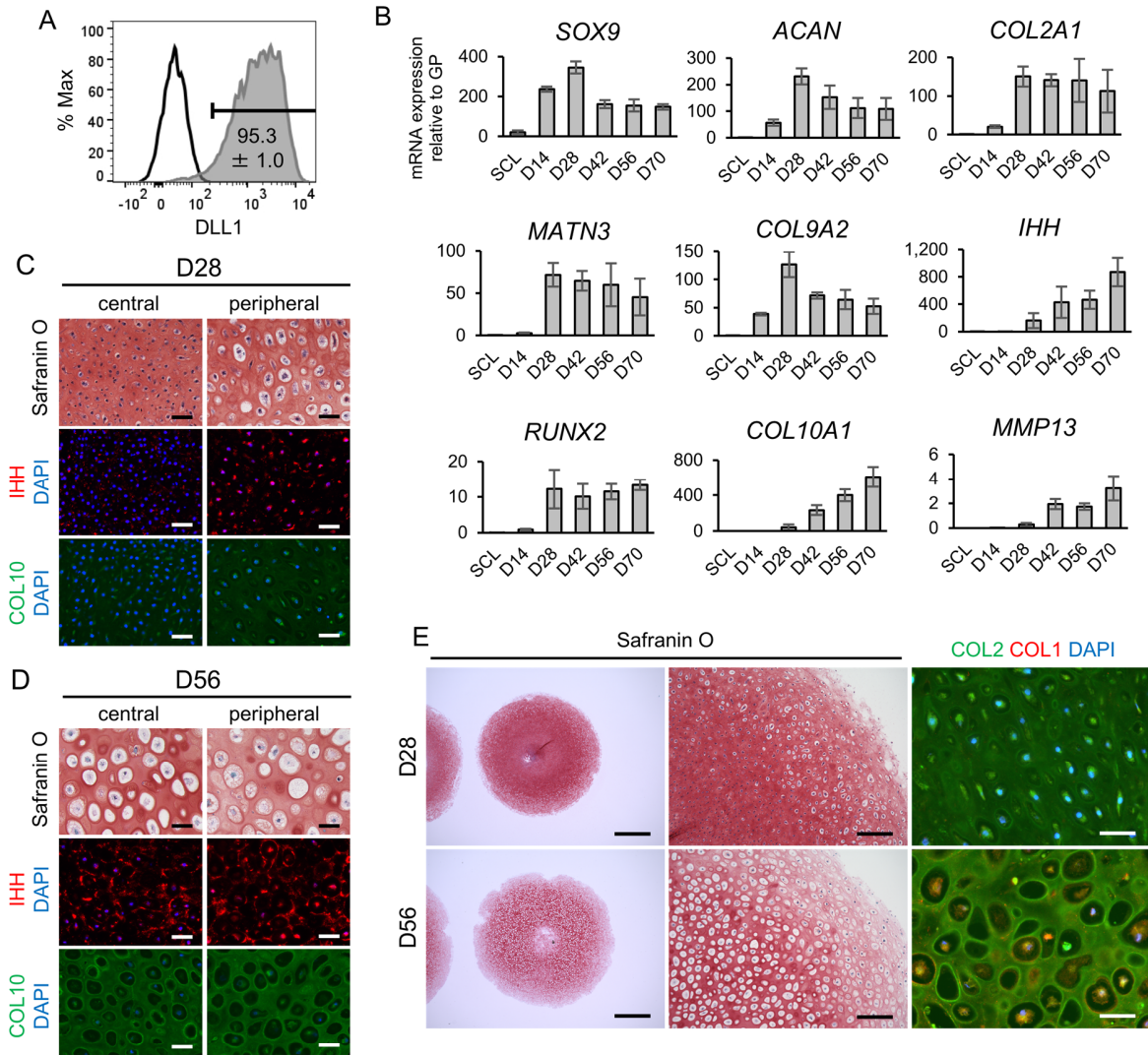
Supplemental Information

**Differentiation of Hypertrophic Chondrocytes from Human iPSCs for
the *In Vitro* Modeling of Chondrodysplasias**

Yann Preteemer, Shunsuke Kawai, Sanae Nagata, Megumi Nishio, Makoto Watanabe, Sakura Tamaki, Cantas Alev, Yoshihiro Yamanaka, Jing-Yi Xue, Zheng Wang, Kenichi Fukiage, Masako Tsukanaka, Tohru Futami, Shiro Ikegawa, and Junya Toguchida

Inventory of Supplemental Information

- Supplemental Figures S1-S6
- Supplemental Tables S1-S6
- Supplemental Experimental Procedures
- Supplemental References



F

expressed tissue	marker	414C2						1231A3						growth plate
		SCL	D14	D28	D42	D56	D70	SCL	D14	D28	D42	D56	D70	
cartilage	ACAN	31.8	22.4	19.3	19.0	19.2	20.1	31.5	21.7	19.3	19.4	19.7	20.3	24.4
	COL2A1	23.4	21.6	17.4	16.3	16.6	17.9	23.4	20.3	17.1	16.5	16.6	17.6	22.1
	COL9A2	27.7	22.3	19.5	19.4	19.5	20.7	28.1	21.5	19.6	19.9	20.1	20.6	23.0
	MATN3	30.2	25.2	20.9	19.6	20.7	23.6	30.6	25.4	20.3	19.8	20.2	21.5	23.9
	SOX9	24.0	24.6	22.7	22.5	22.9	23.7	24.3	23.2	22.3	22.7	22.7	23.3	27.9
hypertrophic cartilage	COL10A1	37.1	34.9	21.4	16.0	15.2	15.5	42.3	34.9	20.4	16.1	15.2	15.1	21.5
	IHH	37.3	34.2	27.3	23.4	23.2	23.8	37.2	32.5	26.4	24.2	23.5	23.2	30.4
	MMP13	u.d.	40.4	31.9	27.5	27.8	27.2	u.d.	37.7	30.5	26.8	26.8	26.5	24.4
	RUNX2	32.8	29.4	25.8	24.5	24.4	24.9	32.8	29.1	25.1	24.7	24.1	24.4	25.5
bone	ALPL	29.6	35.5	23.5	20.3	20.4	22.2	25.9	29.6	22.4	20.1	19.9	20.9	24.0
	COL1A1	23.7	28.9	28.5	28.2	26.7	24.1	23.7	24.7	25.4	23.4	22.1	22.1	19.2
	IBSP	36.0	38.9	27.7	21.6	21.4	21.3	38.9	35.2	28.5	21.4	20.3	20.4	21.1
	SP7	34.6	32.5	25.7	23.1	23.2	23.8	32.9	31.0	25.2	23.6	23.3	23.5	27.1
adipose	CEBPA	35.4	40.6	38.4	39.0	35.5	36.3	35.7	38.0	39.2	37.8	38.3	37.5	30.9
	FABP4	41.4	38.5	34.6	35.6	35.6	35.5	38.0	34.8	32.8	31.6	32.3	30.6	21.8
	PPARG	32.7	35.0	30.2	27.6	27.9	27.6	31.8	33.4	28.5	27.0	25.8	26.2	26.0
ligament	MKX	32.1	25.1	23.9	24.4	25.7	26.5	30.6	23.7	23.7	24.3	24.9	26.1	30.3
	SCX	27.7	25.9	30.1	32.7	32.4	32.4	26.7	25.2	29.1	29.7	30.3	32.1	29.6
	TNMD	31.9	30.7	32.9	33.9	35.7	35.9	31.7	32.5	33.6	35.5	32.8	32.9	29.7
sclerotome	PAX9	24.3	28.7	29.2	30.2	31.5	32.6	24.9	25.3	27.7	28.5	29.2	31.2	33.6
	NKX3-2	25.6	27.8	25.4	25.9	27.7	29.9	25.6	25.4	24.1	24.9	25.9	27.8	29.0
muscle	MYOD1	35.9	36.4	34.9	35.2	35.8	35.8	37.0	34.1	34.8	34.6	34.6	34.9	37.8
ectoderm	SOX1	32.8	32.7	34.5	33.9	33.9	32.5	28.5	29.7	31.9	33.3	32.4	33.1	38.2
endoderm	SOX17	32.9	33.1	29.0	28.4	29.7	31.1	32.3	31.9	27.8	27.6	28.8	29.5	27.9
all	ACTB	18.1	21.7	20.5	19.6	20.1	19.8	17.9	20.5	20.2	19.5	19.4	19.9	17.3

Figure S1. Differentiation of hypertrophic chondrocytes from 1231A3 iPSCs. Related to Figure 1

(A) Representative result of DLL1-positive cells (compared to isotype control) on day 2 of sclerotome induction (SI) with the mean and SEM (standard error of the mean) of n=4 independent experiments displayed.

(B) mRNA expression of chondrocyte markers over time from SCL on day -1 to day 70 of HI by qPCR. Values are shown as mean \pm SEM (n=3 independent experiments), relative to the mean of 6 pieces of a human distal femoral growth plate (GP).

(C, D) Safranin O and IHH or COL10 immunostaining on day 28 (C) and day 56 (D) of HI in the central or peripheral area of each pellet. Scale bars, 50 μ m.

(E) Safranin O staining (left, middle columns) and COL2 (green) with COL1 (red) immunostaining (right column) of pellets from day 28 and 56 of HI. Scale bars, (left column) 1 mm, (middle column) 200 μ m, (right column) 50 μ m.

(F) Ct values of markers of different tissue types from qPCR. Values are the mean from n=4 (414C2) or n=3 (1231A3) independent experiments or 6 pieces of the human distal femoral growth plate. For values indicated in red, the signal was undetected in at least one replicate. u.d., undetected in all replicates. For (C), (D), (E), similar results were obtained in n=4 independent experiments.

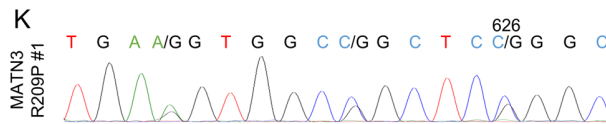
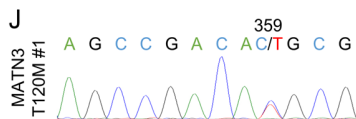
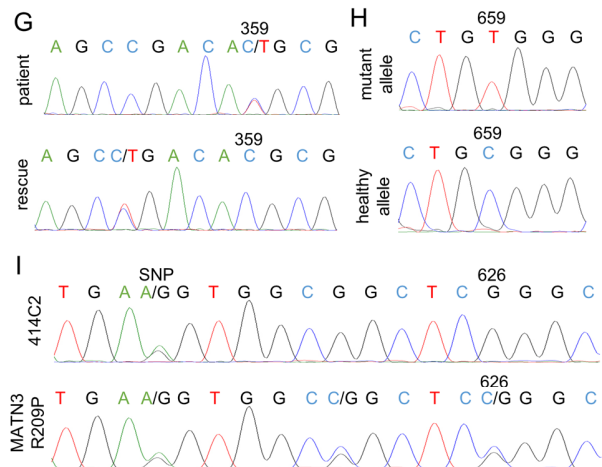
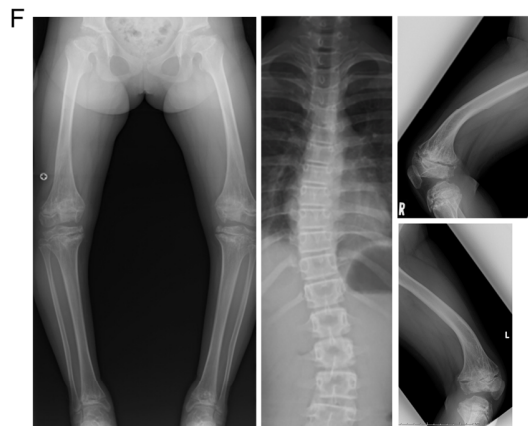
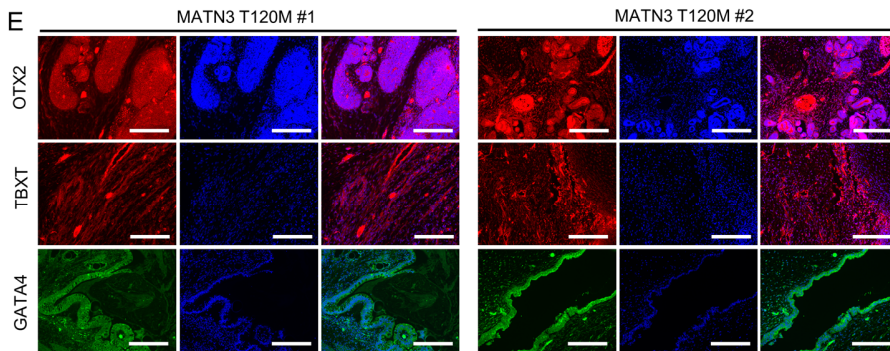
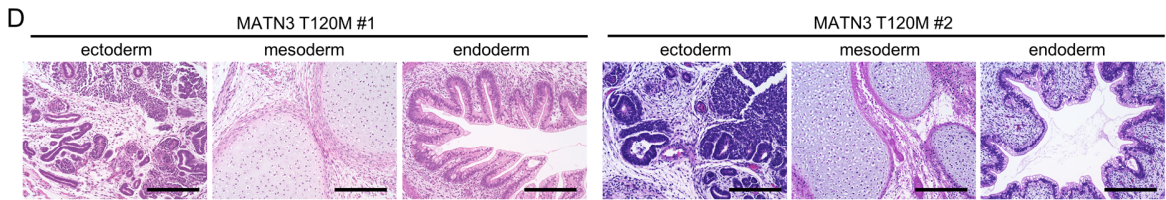
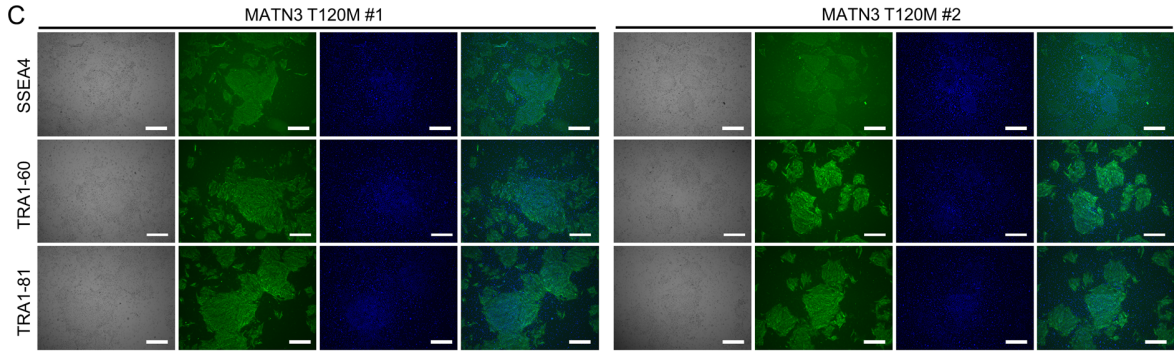
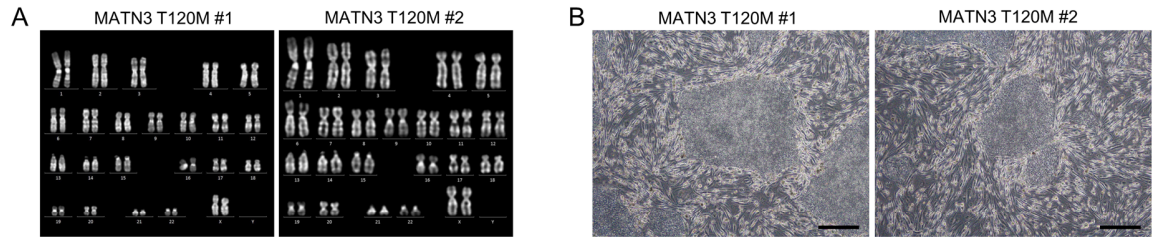


Figure S2. Multiple epiphyseal dysplasia (MED) patient phenotype, validation of iPSC clones and sequence of an additional *MATN3* mutant clone. Related to Figure 2

(A) Karyotype analysis of MED patient-derived clones #1 and #2, showing a normal karyotype of 46,XX.

(B) Phase-contrast image of iPSC clones (on-feeder culture at the time of validation). Scale bars, 100 μ m.

(C) Brightfield image (left) and immunostaining (right) of each clone. Pluripotent markers are shown in green with the nuclear counterstain DAPI in blue. Scale bars, 100 μ m.

(D) HE staining of tissue formed from teratomas of each clone, showing differentiation into ectoderm, mesoderm and endoderm. Scale bars, 200 μ m.

(E) Immunostaining of ectoderm marker OTX2 (red), mesoderm marker TBXT (red), and endoderm marker GATA4 (green) with DAPI (blue) in teratoma tissue. Scale bars, 200 μ m.

(F) Patient x-ray image of the lower limbs (left), spine (middle), right femur (upper right) and left femur (lower right).

(G) Sequence of the patient showing the heterozygous *MATN3* c.359C>T (p.T120M) mutation (top) and the gene-corrected rescue (bottom).

(H) Single allele sequence of the mutant allele (top) and healthy allele (bottom), showing the healthy allele containing the SNP rs187943382, *MATN3* c.659T>C (p.V220A).

(I) Sequence of the wild type iPSC line 414C2 (top), showing the SNP in *MATN3* used for allele-specific targeting, and the mutant 414C2 with the heterozygous *MATN3* c.626G>C (p.R209P) mutation (bottom).

(J, K) Sequence of cDNA reverse-transcribed from RNA on day 56 of HI of the mutant clones showing that the mutant RNA is expressed.

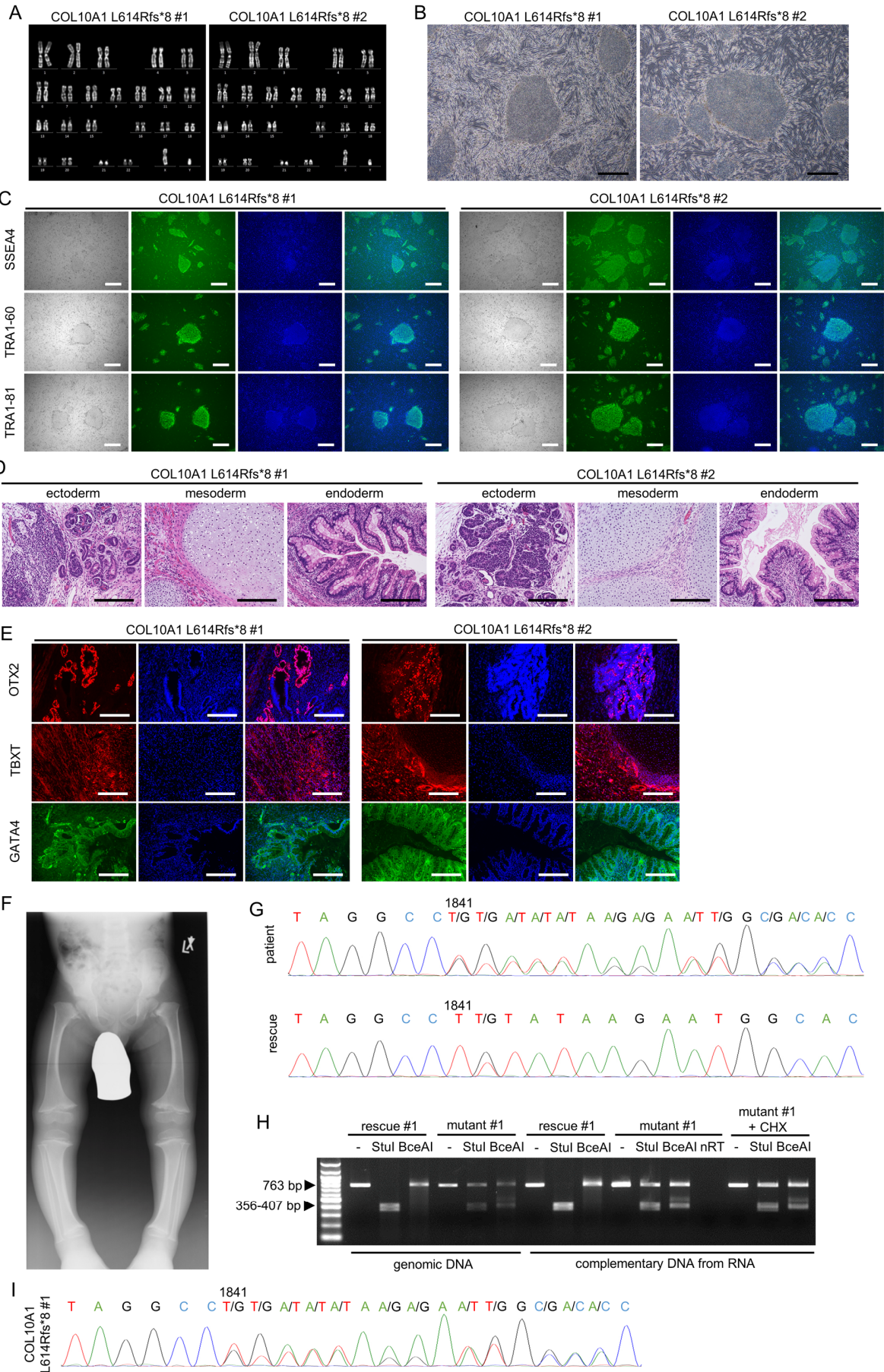


Figure S3. Metaphyseal chondrodysplasia type Schmid (MCDS) patient #1 phenotype and validation of iPSC clones. Related to Figure 2

(A) Karyotype analysis of clones #1 and #2, showing a normal karyotype of 46,XY.

(B) Phase-contrast image of iPSC clones (on-feeder culture at the time of validation). Scale bars, 100 μ m.

(C) Brightfield image (left) and immunostaining (right) of each clone. Pluripotent markers are shown in green with the nuclear counterstain DAPI in blue. Scale bars, 100 μ m.

(D) HE staining of tissue formed from teratomas of each clone, showing differentiation into ectoderm, mesoderm and endoderm. Scale bars, 200 μ m.

(E) Immunostaining of ectoderm marker OTX2 (red), mesoderm marker TBXT (red), and endoderm marker GATA4 (green) with DAPI (blue) in teratoma tissue. Scale bars, 200 μ m.

(F) Patient x-ray image of the lower limbs.

(G) Sequence of the patient showing the heterozygous *COL10A1* c.1841_1841delT (p.L614Rfs*8) mutation (top) and the gene-corrected rescue (bottom).

(H) Electrophoresis after reverse transcribing RNA, amplifying the *COL10A1* region containing the mutation by PCR, and processing the amplicons by restriction enzyme *StuI* (recognizing only the wild type allele) or *BceAI* (recognizing only the mutant allele). The mutant allele is clearly visible and not changed by NMD (nonsense-mediated decay) inhibitor CHX (cycloheximide), showing that the early stop codon in L614Rfs*8 does not lead to NMD. The nRT (no reverse transcriptase) negative control shows no band, indicating that no DNA contamination is present. RNA was taken from samples on day 56 of HI. Similar results were obtained in three biologically independent experiments.

(I) Sequence of cDNA reverse-transcribed from RNA on day 56 of HI of the mutant clone showing that the mutant RNA is expressed.

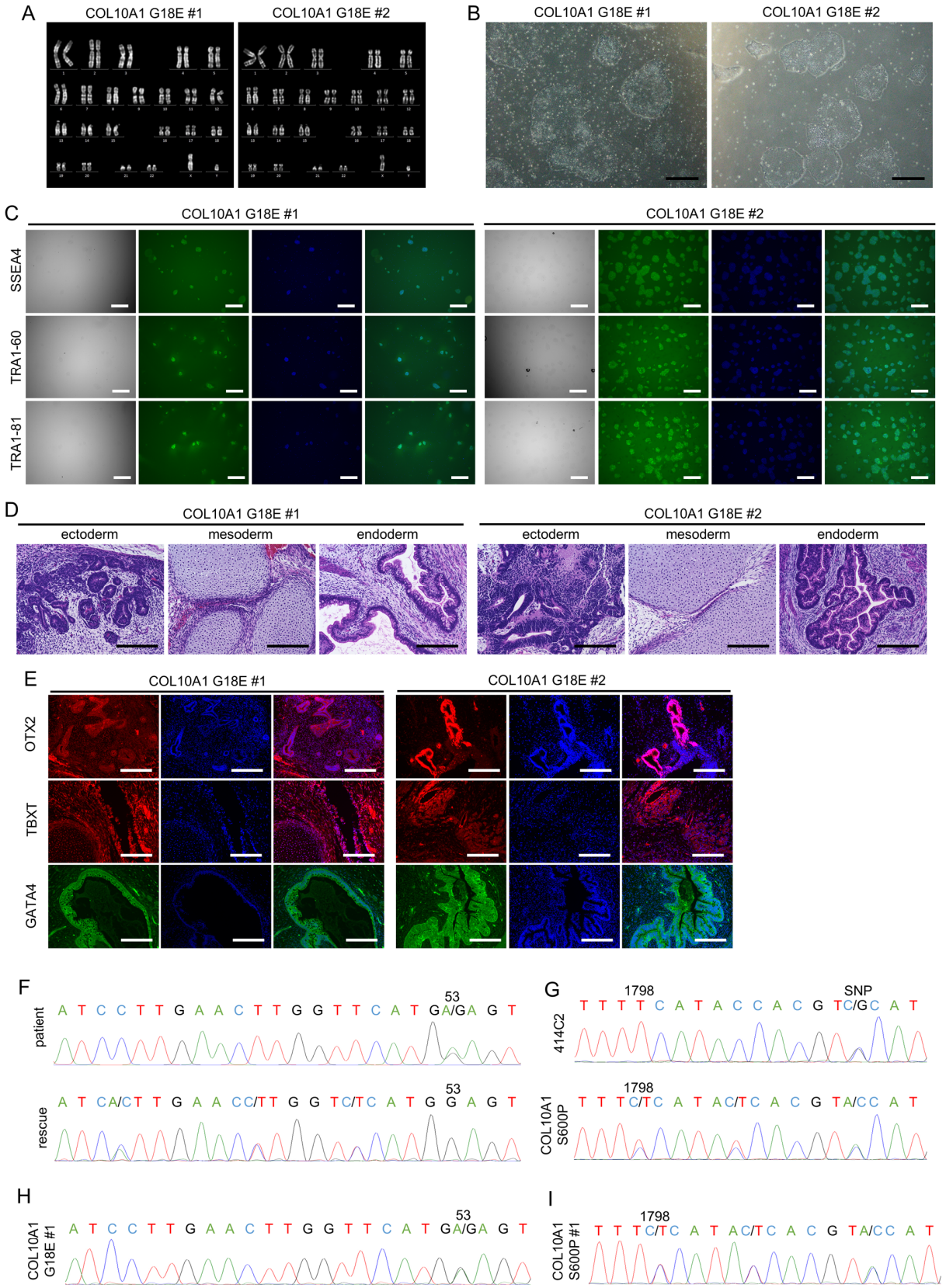


Figure S4. Validation of iPSC clones from MCDS patient #2 and sequence of an additional *COL10A1* mutant clone. Related to Figure 2

(A) Karyotype analysis of clones #1 and #2, showing a normal karyotype of 46,XY.

(B) Phase-contrast image of iPSC clones (feeder-free culture at the time of validation). Scale bars, 100 μ m.

(C) Brightfield image (left) and immunostaining (right) of each clone. Pluripotent markers are shown in green with the nuclear counterstain DAPI in blue. Scale bars, 100 μ m.

(D) HE staining of tissue formed from teratomas of each clone, showing differentiation into ectoderm, mesoderm and endoderm. Scale bars, 200 μ m.

(E) Immunostaining of ectoderm marker OTX2 (red), mesoderm marker TBXT (red), and endoderm marker GATA4 (green) with DAPI (blue) in teratoma tissue. Scale bars, 200 μ m.

(F) Sequence of the patient showing the heterozygous *COL10A1* c.53G>A (p.G18E) mutation (top) and the gene-corrected rescue (bottom).

(G) Sequence of the wild type iPSC line 414C2 (top), showing the SNP in *COL10A1* used for allele-specific targeting, and the mutant 414C2 with the heterozygous *COL10A1* c.1798T>C (p.S600P) mutation (bottom).

(H, I) Sequence of cDNA reverse-transcribed from RNA on day 56 of HI of the mutant clones showing that the mutant RNA is expressed.

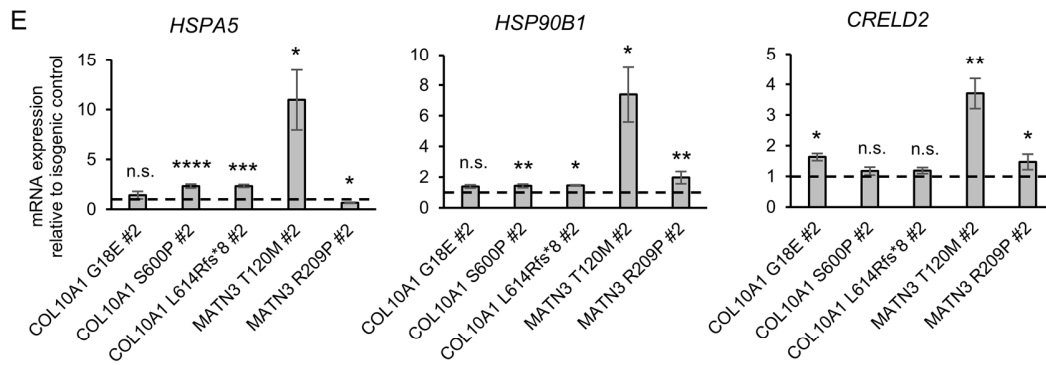
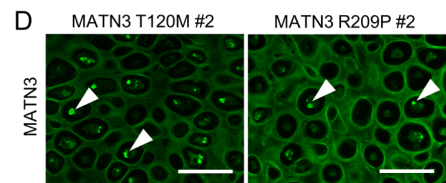
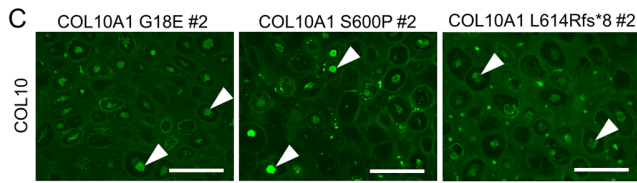
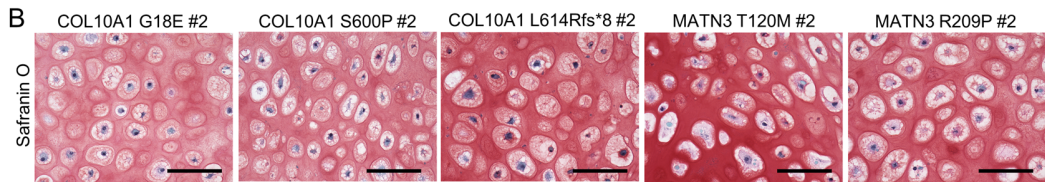
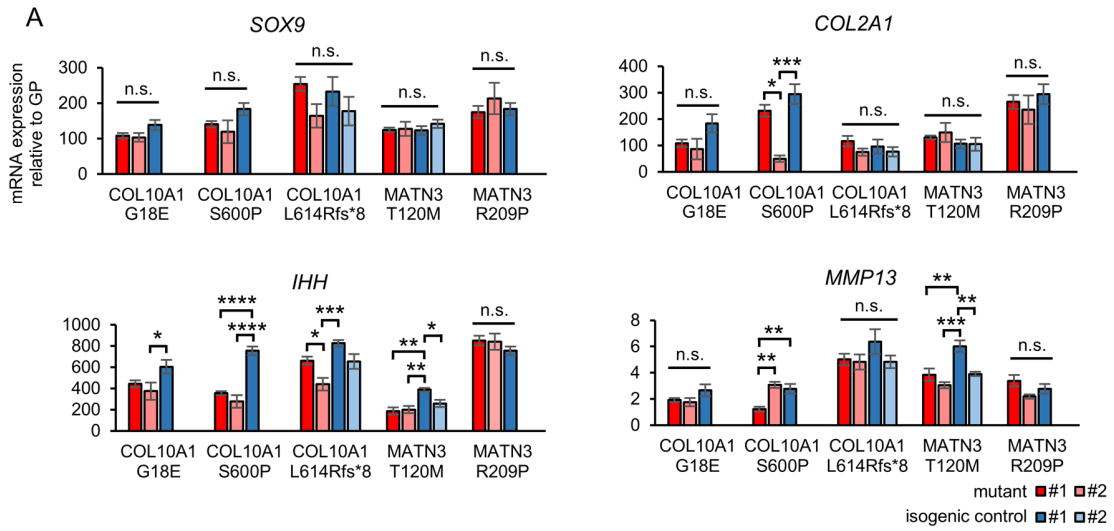


Figure S5. Additional mutant clones also show intracellular retention and ER stress without disruption of chondrogenic differentiation. Related to Figures 2, 3, and 4

(A) mRNA expression of chondrocyte markers of various stages by qPCR. Values are relative to the mean of 6 pieces of the human distal femoral growth plate (number of independent experiments shown in Table S2). Statistical analysis by ANOVA with post-hoc Tukey HSD.

(B) Safranin O staining. Similar results were obtained in n=3 independent experiments. Scale bars, 100 μ m.

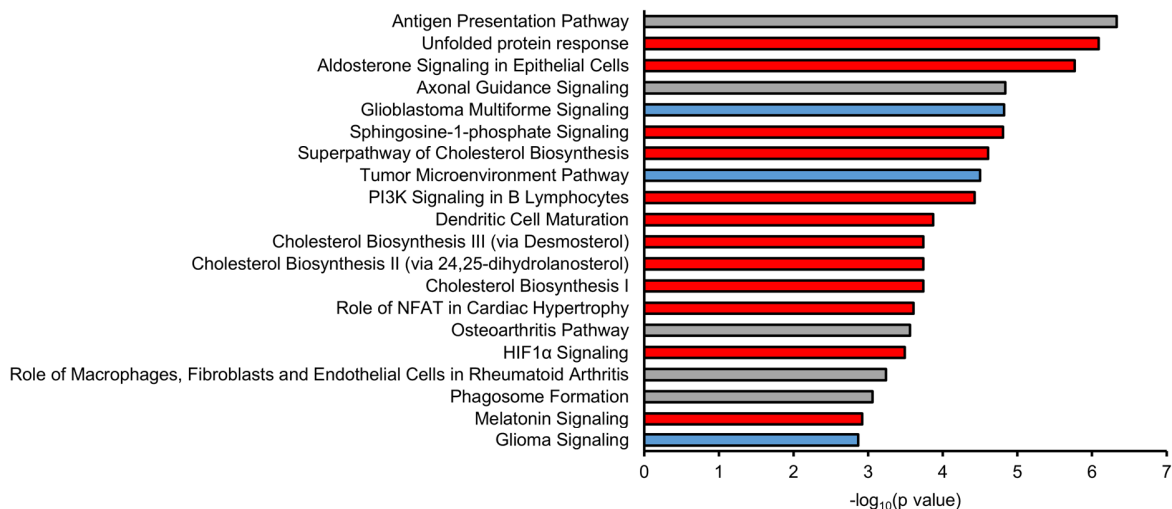
(C, D) Immunostaining of COL10 (C) or MATN3 (D). Similar results were obtained in n=3 independent experiments. Arrowheads indicate intracellular aggregates. Scale bars, 100 μ m.

(E) mRNA expression of ER stress and UPR markers by qPCR. Values are relative to the respective isogenic control (number of independent experiments shown in Table S2). Dotted lines indicate the value=1 of the isogenic controls. Statistical analysis by unpaired two-sided t-test.

All results are from day 56 of HI and expressed as the mean \pm SEM. (n.s. no significant difference, *p < 0.05, **p < 0.01, ***p < 0.001, ****p < 0.0001).

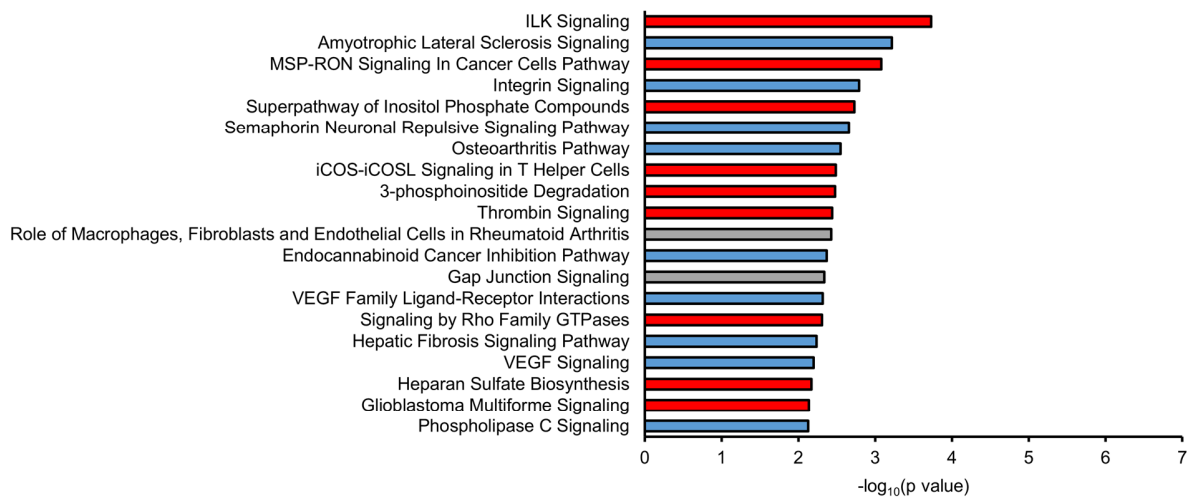
A

Top 20 affected canonical pathways in MATN3 T120M



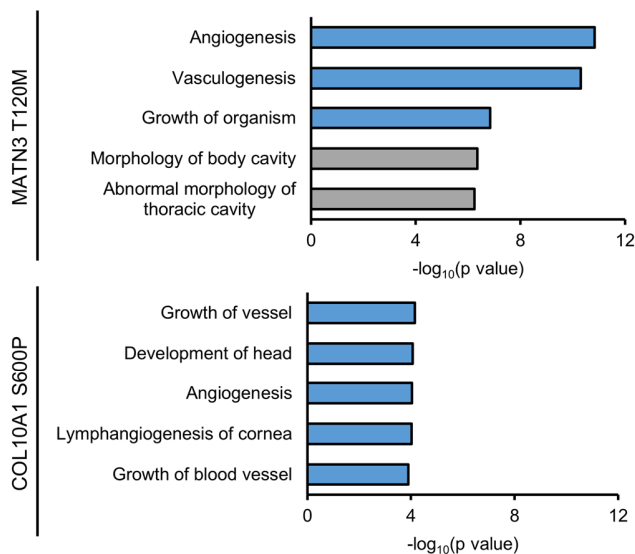
B

Top 20 affected canonical pathways in COL10A1 S600P



C

Organismal Development: Top 5



D

Small Molecule Biochemistry: Top 5

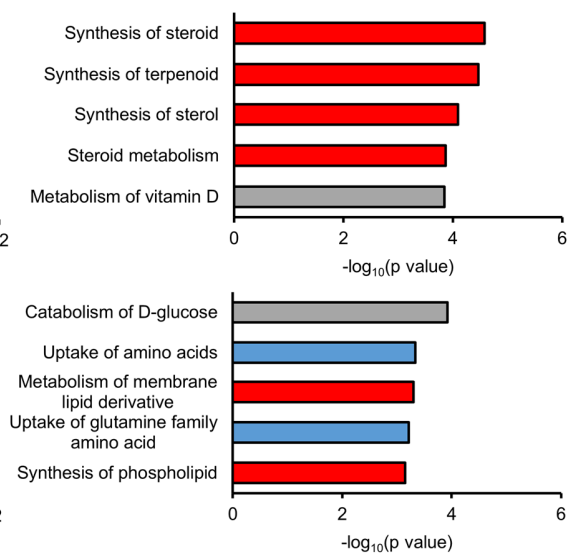


Figure S6. Different pathways and functions are affected in the MATN3 T120M and COL10A1 S600P mutants. Related to Figure 6

(A, B) Top 20 IPA Canonical Pathways in the MATN3 T120M and COL10A1 S600P mutants vs their isogenic controls by microarray analysis (n=3 independent experiments).

(C, D) Top 5 Organismal Development (C) and Small Molecule Biochemistry (D) terms in IPA Diseases and Functions for the MATN3 T120M (top) and COL10A1 S600P (bottom) mutants vs their isogenic controls by microarray analysis (n=3 independent experiments).

All results are from day 56 of HI. Genes with adjusted p value < 0.05 by moderated t-test were used for IPA. Red bars, positive activation z-score; blue bars, negative activation z-score; gray bars, zero or unavailable activation z-score.

Supplemental Tables

Table S1. Transcriptome analysis details. Related to Figures 1 and 6

(see Table S1.xlsx)

Table S2. Number of independent experiments for mRNA expression in Figures 2B, 4F, 4G, and Supplemental Figures S5A, S5E

Sample name	Mutant or isogenic control	Number of independent experiments
COL10A1 G18E	mutant (#1)	12
	mutant #2	4
	isogenic control (#1)	8
COL10A1 S600P	mutant (#1)	12
	mutant #2	4
	isogenic control (#1)	12
COL10A1 L614Rfs*8	mutant (#1)	8
	mutant #2	4
	isogenic control (#1)	4
	isogenic control #2	4
MATN3 T120M	mutant (#1)	4
	mutant #2	4
	isogenic control (#1)	4
	isogenic control #2	4
MATN3 R209P	mutant (#1)	8
	mutant #2	4
	isogenic control (#1)	12

^aUnless stated otherwise, all mutants and isogenic controls in the main and supplemental figures refer to mutants #1 and isogenic controls #1.

Table S3. Guide RNAs and repair templates used for gene editing. Related to Experimental Procedures

Gene editing	Guide RNA (protospacer)	Single-stranded oligonucleotide repair template (100 nt)	Restriction enzyme
Creation of COL10A1 S600P	CGTGCATGTGAA AGGGACTC	CCCAAGGACTGGAATCTTTACTTGT CAGATACCAGGAATATACTATTTTCCATATCAC GT <u>ACATGT</u> GAAAGGGACTCATGTTTGGG TAGGCCTGTATAAG	PciI (ACATGT)
Creation of MATN3 R209P	AGGTGAATGAAG TGGCGGCT	ATCATTGTTACAGATGGGAGGCCCCAGG ACCAGGTGAATGAAGTGG <u>CCGCTCCGG</u> CCCAAGCATCTGGTATTGAGCTCTATGC TGTGGGCGTGGACCGG	BsrBI (CCGCTC)
Rescue of COL10A1 G18E	TGAACTTGGTTCA TGAAGTG	AGAATATGCTGCCACAAATACCCTTTTTG CTGCTAGTATCATTGAACCTGGT <u>CCATG</u> <u>GAGT</u> GTTTTACGCTGAACGATACCAAAT GCCACAGGCATAAA	NcoI (CCATGG)
Rescue of COL10A1 L614Rfs*8	TTGGGTAGGCCG TATAAGAA	TTCATACCACGTGCATGTGAAAGGGACT CATGTTTGGGTAGGCCTT <u>TATA</u> AAGATG GCACCCCTGTAATGTACACCTATGATGA ATACACCAAAGGCTAC	PsiI (TTATAA)
Rescue of MATN3 T120M	ACATGCGGGTGG CAGTGGTG	AACTTTTGTCTCCCGGATAATCGACACT CTGGACATTGGGCC <u>CAGCTG</u> ACACGCGG GTGGCAGTGGTGAACCTATGCTAGCACTG TGAAGATCGAGTTCCAA	PvuII (CAGCTG)

^aUnderlined nucleotides in the repair template indicate the recognition sites of the restriction enzymes.

Table S4. Primers for sequencing. Related to Experimental Procedures

Amplified domain	Direction	Sequence
COL10A1 NC1 domain	forward	CAGCAGGAGCAAAGGGAATG
	forward	GCTGGCATAGCAACTAAGG
	forward	CCACCAGGTCAAGCAGTCATG
	reverse	TTGAATGGGAGGCACAAGG
	reverse	GGGAAGGTTTGTGCTG
	reverse	TGTACTIONCACATTGGAGCCACTAG
COL10A1 NC2 domain	forward	TCAGTCTGTGGATGATAGTC
	forward	CACTTGATTACCTGAGTATAGC
	forward	CAAGGCACCATCTCCAGGAAC
	forward	CATCTCCAGGAACTCCCAGC
	reverse	AGTTTCATTTGCCTGCTTG
	reverse	CAGAAGTTGGAAAGTAACACC
	reverse	TATGGTCCTCTCTCCTGG
	reverse	CCTTGCTCTCCTCTTACTGC
MATN3 vWFa domain	forward	GCAGAGGGATGAGGTTCTAAG
	forward	GCAGGCAGTGGTGATGTTGG
	forward	AGATAAGCAGTCCCTGAAGC
	forward	GACTIONCCTCCTGCTGCTCTGG
	reverse	GTTGGAAGCAAAGACTGACC
	reverse	GGCTTCGTCCATTGCTGTCTG
	reverse	TCACAGTGGTGCTTGCCCTTC

Table S5. Primers for qPCR. Related to Experimental Procedures

Amplified gene	Direction	Sequence
ACTB	forward	CACCATTGGCAATGAGCGGTTTC
	reverse	AGGTCTTTGCGGATGTCCACGT
COL10A1	forward	CCCAGCACGCAGAATCCATC
	reverse	AGTGGGCCTTTTATGCCTGT
COL2A1	forward	CGAGGCAACGATGGTCAGCC
	reverse	TGGGGCCTTGTTACCTTTGA
MATN3	forward	GTTCAGTCCGTGACAAGTGTG
	reverse	AGTCTTCGTGCTTCCTCAGTG
SOX9	forward	GACTTCCGCGACGTGGAC
	reverse	GTTGGGCGGCAGGACTG
MMP13	forward	CATGAGTTCGGCCACTCCTT
	reverse	CCTGGACCATAGAGAGACTGGA
IHH	forward	CGGTGGACATCACCACATCA
	reverse	CGTGGGCCTTTGACTCGTAA
ALPL	forward	GGAAGACTCTGACCGTGG
	reverse	GGGGGCCAGACCAAAGATAG
SP7	forward	ATCCAGCCCCCTTTACAAGC
	reverse	TAGCATAGCCTGAGGTGGGT
ACAN	forward	TCGAGGACAGCGAGGCC
	reverse	TCGAGGGTGTAGCGTGTAGAGA
RUNX2	forward	TTACTTACACCCCGCCAGTC
	reverse	TATGGAGTGCTGCTGGTCTG
COL9A2	forward	GCGCTATCGGTGCCACTGGG
	reverse	GGGGGCCCGTTGCTCCTTTC
HSPA5	forward	GTTTGCTGAGGAAGACAAAAGCTC
	reverse	CACTTCCATAGAGTTTGCTGATAATTG
CRELD2	forward	CCAAGTACGAGTCCAGCGAG
	reverse	TGCTCCTCCTGCGCCTCTAG
HSP90B1	forward	ATGGAGCAGCAAGACTGAAAC
	reverse	TCTTCTTCTTCTCCTCTACTGC
XBP1 spliced	forward	TGCTGAGTCCGCAGCAGGTG
	reverse	GCTGGCAGGCTCTGGGGAAG
EDEM3	forward	GATGGAGAAGGATGAGCTATGAC
	reverse	GAACGTGGTTGTTTCATCACC
DERL3	forward	CCTCGTGGACCTGCTGG
	reverse	GGTCTGCAGGAGCCTCTTG

HERPUD1	forward	CGTTGTTATGTACCTGCATC
	reverse	TCAGGAGGAGGACCATCATTT
COL1A1	forward	GGACACAGAGGTTTCAGTGGT
	reverse	GCACCATCATTTCCACGAGC
IBSP	forward	AAGGACAAGGCTACGATGGC
	reverse	CGGATGCAAAGCCAGAATGG
CEBPA	forward	CGGTGGACAAGAACAGCAAC
	reverse	CGGAATCTCCTAGTCCTGGC
FABP4	forward	ACCAGGAAAGTGGCTGGCAT
	reverse	CAGGTCAACGTCCCTTGGCT
PPARG	forward	GCTGTTATGGGTGAAACTCTG
	reverse	ATAAGGTGGAGATGCAGGCTC
MKX	forward	CGCACAGACACTCTGGAAAA
	reverse	AGCGGCACTTTGACAGTCTT
SCX	forward	CCCAAACAGATCTGCACCTTC
	reverse	GCGAATCGCTGTCTTTCTGTC
TNMD	forward	CCATGCTGGATGAGAGAGGT
	reverse	CTCGTCCTCCTTGGTAGCAG
PAX9	forward	ACAGTGCTGCTCCTTCTGGT
	reverse	ATGTGAGACCTGGGAATTGG
NKX3-2	forward	CAGAAATTCTCCAAAGATGC
	reverse	TCTCCCTACAGTTTCGCCG
MYOD1	forward	GTGTGAGCCTAGACTGCCT
	reverse	CTCAGAAGGCACGTCCGC
SOX1	forward	TACAGCCCATCTCCAATC
	reverse	GCTCCGACTTCACCAGAGAG
SOX17	forward	CGCTTTCATGGTGTGGGCTAAGGACG
	reverse	TAGTTGGGGTGGTCTGCATGTGCTG

Table S6. Key reagents used in this study. Related to Experimental Procedures

Induction reagents and drugs	Source	Identifier
AK02N	Ajinomoto	AJ100
iMatrix-511 silk	Nippi	892021
Matrigel	BD	354230
PenStrep	Gibco	15140-163
bFGF	Wako	068-04544
CHIR99021	Axon	Axon1386
Activin A	R&D	338-AC01-M
SB431542	Selleck Chemicals	S1067
LDN193189	Stemgent	04-0074
PD173074	Tocris	3044
XAV939	Tocris	3748/10
SAG	Calbio	566660
Y-27632	Wako	034-24024
Ham's F12	Gibco	11765-054
BSA	Sigma	A8806-5G
IMDM	Sigma	I3390
CD Lipid	Life Tech	11905-031
Apo-transferrin	Sigma	T1147-500MG
Monothioglycerol	Sigma	M6145-25ML
Insulin	Wako	097-06474
Dexamethasone	Wako	047-18863
PDGF-BB	R&D	520-BB
TGF β 3	R&D	243-B3
BMP4	R&D	314-BP
T3	Sigma	T-074-1ML
β -glycerophosphate	Sigma	G6501-100G
ITS premix	Corning	354352
L-ascorbic acid 2-phosphate	Sigma	A8960
Proline	Sigma	P-5607
Glucose	Sigma	G8769
Sodium pyruvate	Sigma	S8636

Glutamax	Life Tech		35050-061	
DMEM/F12	Gibco		11320-033	
Carbamazepine	Sigma		C4024-1G	
Trimethylamine N-oxide	Sigma		317594-5G	
Valproic acid	Sigma		P4543-10G	
Rapamycin	MedChemExpress		HY10219	
Antibodies	Host	Clonality	Source	Identifier
COL1	Rabbit	Polyclonal	Novus Biologicals	NB600-408-0.1mg
COL2	Mouse	Monoclonal	Thermo	MS235P0
COL10	Mouse	Monoclonal	Thermo	14-9771-82
MATN3	Rabbit	Polyclonal	abcam	ab106388
PDI	Mouse	Monoclonal	Thermo	MA3-019-A647
IHH	Rabbit	Polyclonal	abcam	ab39634
COL1	Goat	Polyclonal	SBA	1310-01
COL2	Goat	Polyclonal	SBA	1320-01
Ki67	Rabbit	Monoclonal	Nichirei	718071
DLL1	Mouse	Monoclonal	R&D	FAB1818A
APC-conjugated mouse IgG2B	Mouse	Monoclonal	R&D	IC0041A
SSEA4	Mouse	Monoclonal	Chemicon	MAB4304
TRA1-60	Mouse	Monoclonal	Chemicon	MAB4360
TRA1-81	Mouse	Monoclonal	Chemicon	MAB4381
OTX2, TBXT, GATA4	Goat	Polyclonal	R&D	SC022
ATF6	Mouse	Monoclonal	abcam	ab122897
ACTB, peroxidase conjugate	Mouse	Monoclonal	Sigma	A3854-200UL
Phospho-EIF2A	Rabbit	Monoclonal	CST	3398T
EIF2A	Rabbit	Monoclonal	CST	5324T
ACTB	Rabbit	Monoclonal	CST	4970S
HSPA5	Rabbit	Monoclonal	CST	3177T
PDI	Rabbit	Monoclonal	CST	3501T
ERO1A	Rabbit	Polyclonal	CST	3264T

Supplemental Experimental Procedures

Establishment of isogenic iPSC lines using CRISPR/Cas9

In order to create gene-corrected rescues, the 20 nt protospacer sequence for the guide RNA targeting the mutated site was inserted into the vector pSpCas9(BB)-2A-Puro (PX459) V2.0 (Addgene). Cloning was performed as previously described¹ using DH5 α cells (Toyobo). The vector was isolated using the Midi Prep Kit (Macherey-Nagel) and electroporated into iPSCs (1×10^6 cells) using the NEPA 21 (Nepa Gene), together with a repair template consisting of 100 nt including the gene correction, a recognition site for restriction enzymes to confirm the insertion, and silent mutations for PAM or guide RNA blocking. Cells were cultured in six well plates with 10 μ M Y-27632 overnight, after which they were treated with 0.5-0.7 μ g/ml puromycin for 24 hours to select for cells incorporating the vector. One week after sparsely re-seeding the cells, 48-96 single colonies were randomly picked and expanded. Genomic DNA was extracted using the DNeasy Blood and Tissue Kit (QIAGEN) with proteinase K treatment, upon which the relevant regions were amplified with PCR using KOD Plus Neo (Toyobo). Amplicons were digested by the restriction enzymes to confirm insertion of the repair template. Samples for which insertion was confirmed were then purified using the FastGene Gel/PCR Extraction kit (Nippon Genetics) and sequenced using the BigDye Terminator v3.1 Cycle Sequencing Kit (Applied Biosystems) with the 3500xL Genetic Analyzer (Applied Biosystems).

Mutants were established from the wild type iPSC line 414C2 similarly to the gene-corrected rescues. Here, the guide RNA was designed to target a SNP near the intended site of mutagenesis. The 100 nt repair template included the new mutation, a recognition site for restriction enzymes, and silent mutations for PAM or guide RNA blocking. All primers, guide RNAs, repair templates, and restriction enzymes used in this gene editing are listed in Tables S3 and S4.

iPSC culture and validation

All patient-derived iPSC lines were established on SNL feeder cells in primate embryonic stem cell medium (ReproCELL) supplemented with 4 ng/ml bFGF (Wako), 50 U penicillin and 50 μ g/ml streptomycin (Gibco). After several passages as whole colonies on feeder cells, iPSCs were moved to feeder-free culture on dishes coated with laminin (Nippi) in StemFit AK02N (Ajinomoto) and passaged as single cells once a week at a density of 1.1×10^3 to 3.2×10^3 cells/cm².

Newly established iPSC clones were validated for pluripotency by immunostaining either before switching to feeder-free culture (MATN3 T120M and COL10A1 L614Rfs*8) or after the switch (COL10A1 G18E). After fixation in 4% paraformaldehyde, cells were PBS washed and incubated for

1 hour at 4°C in a blocking solution of PBS with 0.2% TritonX-100 (Sigma) and 5% Blocking One Histo (Nacalai Tesque). Pluripotency markers SSEA4, TRA1-60, and TRA1-81 (all Chemicon) were diluted in the blocking solution at 1:400, 1:1000, and 1:1000, respectively, and used to stain the cells overnight at 4°C. On the next day, cells were further incubated for 1 hour at 4°C in blocking solution containing Alexa 488-conjugated goat anti-mouse IgG antibody (Thermo) at 1:500. The nucleus was counterstained using DAPI.

All iPSC clones were further validated for their ability to differentiate into all three germ layers through teratoma formation. 1×10^6 cells were injected into each testis of at least three NOD-SCID mice, which were sacrificed after 8 to 12 weeks to excise the tissue. After fixation in 4% paraformaldehyde, the tissue was embedded in paraffin, sectioned, and stained with H&E. Markers for the three germ layers were stained using the Human Three Germ Layer 3-Color Immunocytochemistry Kit (R&D) according to the manufacturer's instructions.

Sclerotome induction (SI) and hypertrophic chondrocyte induction (HI)

For SI, CDMi (chemically defined medium with insulin) was used as base medium.² This medium consists of a 1:1 mixture of Iscove's modified Dulbecco's medium (IMDM) (Sigma) and Ham's F12 (Gibco), 5 mg/ml BSA (Sigma), 1x CD Lipid (Life Tech), 15 µg/ml apo-transferrin (Sigma), 450 µM monothioglycerol (Sigma), 50 U penicillin, 50 µg/ml streptomycin, and 7 µg/ml insulin (Wako). SI was performed as previously described.³ In brief, on day 0 of induction, primitive streak cells were induced with 20 ng/ml bFGF, 10 µM CHIR99021 (Axon), and 50 ng/ml Activin A (R&D) for 24 hours. Then, presomitic mesoderm cells were induced with 10 µM SB431542 (Selleck Chemicals), 3 µM CHIR99021, 250 nM LDN193189 (Stemgent), and 20 ng/ml bFGF for 24 hours. Following this, somitic mesoderm cells were induced with 100 nM PD173074 (Tocris) and 1 µM XAV939 (Tocris) for 24 hours. Finally, sclerotome cells were induced with 100 nM SAG (Calbio) and 600 nM LDN193189 for 72 hours.

For HI, we used the same basal chondrogenic medium as previously described,⁴ except for the lack of dexamethasone. This medium consists of 1% (v/v) ITS premix (Corning), 0.17 mM L-ascorbic acid 2-phosphate (Sigma), 0.35 mM proline (Sigma), 0.15% (v/v) glucose (Sigma), 1 mM sodium pyruvate (Sigma), 2 mM Glutamax (Life Tech), 100 U penicillin, and 100 µg/ml streptomycin in DMEM/F12 (Gibco). To this medium, the factors described in the Experimental Procedures were sequentially added, and the medium was changed every 2-3 days.

mRNA expression analysis

For RNA extraction, cartilage pellets were first powderized using the Multi-beads shocker (Yasui

Kikai). Total RNA was extracted using the RNeasy Micro or Mini Kit (QIAGEN) with DNase treatment and reverse transcribed using ReverTra Ace (Toyobo) in a total volume of 20 μ L with up to 300 ng of RNA. cDNA was diluted 1:10 and quantitative PCR (qPCR) was performed with 1 μ L cDNA in duplicate reactions using the Thunderbird SYBR qPCR Mix (Toyobo) and QuantStudio 12K Flex Real-Time PCR System (Thermo). Primers are listed in Table S5. All results were normalized by the β -actin expression in each sample. For statistical analysis, unpaired two-sided t-tests were performed for comparisons between two groups. For comparisons between more than two groups, ANOVA with post-hoc Tukey HSD was used. Normal human growth plate tissue was obtained from the distal femoral physis of an 11-year-old female patient with a malignant bone tumor after total femoral replacement and used as control for differentiation markers.

Nonsense-mediated decay (NMD) detection

Genomic DNA was extracted from iPSCs and RNA was extracted on day 56 of HI of the COL10A1 L614Rfs*8 mutant and isogenic control. For the cycloheximide (CHX)-treated group, cartilage pellets were treated with 100 μ g/ml CHX (Sigma) for 6 hours before RNA extraction. RNA was reverse transcribed with a negative control (no reverse transcriptase), and the cDNA was amplified for the NC1 domain with PCR. The amplicons were digested by the restriction enzyme *Stu*I (NEB), which only recognizes the wild type sequence, and *Bce*AI (NEB), which only recognizes the mutant sequence.

Protein expression analysis

On day 56 of HI, cartilage pellets were collected, PBS washed, and stored at -80°C. After adding 100 μ L SDS sample buffer with 1% (v/v) protease inhibitor cocktail (Nacalai Tesque), the pellets were homogenized using homogenizer pestles (Kenis) and sonicated until complete dissolution. The samples were centrifuged and the supernatant was collected. Protein concentration was measured using the Pierce BCA Protein Assay Kit (Thermo). HSPA5, PDI, and ERO1A protein expression was detected with Simple Western (Wes) using the 12-230 kDa Separation Module (ProteinSimple) according to the manufacturer's instructions. For each lane, 5 μ g of protein was used at a concentration of 1 μ g/ μ L and antibodies were used at 1:50 for HSPA5, PDI, or ERO1A and at 1:100 for β -actin (all CST). All results were normalized by the β -actin values of each sample. ATF6, EIF2A, and phospho-EIF2A protein expression was detected using Western blotting. 12 μ g of protein was used per lane of 10% polyacrylamide gel at a concentration of 2 μ g/ μ L. After SDS-PAGE and transfer to PVDF membranes, blocking was performed for 1 hour using 5% skim milk (Nacalai) or 3% polyvinylpyrrolidone (Sigma). Primary antibodies were used at 1:1000 in 5% skim milk or Can Get

Signal 1 (Toyobo) for overnight staining with shaking at 4°C. The secondary antibodies, HRP-conjugated goat anti-rabbit or horse anti-mouse IgG (both CST), were used at 1:5000 in 5% skim milk or Can Get Signal 2 (Toyobo) for 1 hour at room temperature while shaking. The ECL Prime Western Blotting Detection Reagent (GE Healthcare) and the BIO-RAD Chemidoc XRS+ were used to detect the signal. After detection, membranes were stripped of the antibodies using WB Stripping Solution (Nacalai), stained with peroxidase-conjugated β -actin antibody (Sigma), and visualized as above. The signal intensities were quantified using ImageJ. For statistical analysis, unpaired two-sided t-tests were performed.

Microarray analysis

After RNA extraction, RNA quality was confirmed using the RNA 6000 Nano Kit (Agilent Technologies). The RNA was reverse transcribed into cDNA and amplified with the Ambion WT Expression Kit, fragmented and labeled with the GeneChip WT Terminal Labeling and Controls kit, and hybridized to Human Gene 1.0ST Arrays using the GeneChip Hybridization Wash and Stain Kit according to the manufacturer's protocol (Affymetrix). The arrays were scanned and the raw data were imported into GeneSpring GX 14.9 for analysis. The data were normalized using the RMA-16 algorithm and the baseline was adjusted to the median of all samples. A moderated t-test was performed on all samples (n=3 independent experiments) to stabilize the variance estimate in the low number of replicates.⁵ The Benjamini-Hochberg correction was used to account for multiple testing. For Figure 1, all genes with adjusted p value < 0.05 and fold change > 1.5 in day 56 vs day 28 pellets were used for Ingenuity Pathway Analysis (IPA). In IPA, Canonical Pathways and Diseases & Functions were analyzed. Heatmaps were generated in Genespring using the averaged normalized intensity values for each sample. For Figure 6, all genes with adjusted p value < 0.05 were used for IPA. Heatmaps were generated in Microsoft Excel using each mutant's log2 fold change of UPR genes.

Flow cytometry analysis

To determine the induction efficiency of presomitic mesoderm, cells were analyzed by flow cytometry on day 2 of SI. Cells were detached and washed with FACS buffer containing 0.1% (w/v) BSA in PBS. Approximately 5×10^5 cells were stained with either APC-conjugated DLL1 antibody (R&D) or APC-conjugated mouse IgG2B (R&D) as isotype at a 1:200 dilution in FACS buffer for 30 minutes at 4°C. Following another wash with FACS buffer, the cells were stained with 1 μ g/ml DAPI (R&D) to label dead cells. Analysis was performed using the FACS Aria II and the FACSDiva software (BD). Graphs were created using the FlowJo software. For statistical analysis, unpaired two-sided t-

tests were performed.

Histological analysis

Paraffin-embedded tissue sections were deparaffinized and stained with H&E, von Kossa, and Safranin O. TUNEL staining was performed using the ApopTag Peroxidase *In Situ* Apoptosis Detection kit (Millipore) with proteinase K treatment according to the manufacturer's instructions. For immunofluorescence staining, antigen retrieval was performed by 40 minutes incubation at 37°C in 10 mg/ml hyaluronidase (Sigma) and 15 minutes incubation at 80°C in 1 mM EDTA (Wako). After blocking in 10% FBS (Nichirei) for 1 hour, the tissue was stained at 4°C overnight using antibodies against COL1 (Novus Biologicals) at 1:600, COL2 (Thermo) at 1:1000, COL10 (Thermo) at 1:300, IHH (abcam) at 1:800, and MATN3 (abcam) at 1:500 in Can Get Signal Immunostain Solution B (Toyobo). On the next day, the samples were incubated at room temperature for 1 hour in the same solution with Alexa 488-conjugated goat anti-mouse IgG antibody (Thermo) at 1:1000, Alexa 555-conjugated goat anti-rabbit IgG antibody (Thermo) at 1:1000, Alexa 647-conjugated donkey anti-mouse IgG antibody (Thermo) at 1:1000, and Alexa 647-conjugated PDI antibody (Thermo) at 1:500. DAPI was used as a nuclear counterstain at 10 µg/ml and the samples were observed with the BZ-X810 (Keyence). For immunohistochemistry, antigen retrieval was performed by 40 minutes incubation in EDTA at 98°C or 5 minutes incubation in proteinase K at room temperature, and blocking was performed using 3% BSA. Samples were incubated for 30 minutes at room temperature with antibodies against Ki67 (Nichirei), or overnight at 4°C with antibodies against COL1 (SBA) at 1:500, COL2 (SBA) at 1:600, or HSPA5 (CST) at 1:1600. Simple Stain MAX PO (R) or (G) (Nichirei) was used to detect the signal.

Image analysis and quantification

All samples were quantified using the BZ-X800 Analyzer software and statistical analysis was performed using unpaired two-sided t-tests. Pellet size was quantified using images taken of live pellets from 3 technical replicates each of 4 independent experiments on day 56 of HI with the BZ-X810 (Keyence). The size was calculated by taking the average of the major axis of each pellet.

For quantification of the COL2 and TUNEL stainings, 4 images each were taken of 4 independent experiments at x20 magnification, with the images being taken at the top, bottom, left, and right sides of the pellet, at a depth of approximately 500-1000 µm from the surface to avoid both the necrotic center and the disintegrating periphery. Dead cells of each sample were quantified by counting the number of TUNEL-positive cells per field of view (FOV). Cell size was quantified by selecting the inverse of COL2 staining and measuring the average area of the selection.

For the quantification of COL10, MATN3, and PDI stainings, 4 images each were taken of 4 independent experiments at x40 magnification randomly throughout the pellet at a depth of approximately 500-1000 μm from the surface to avoid both the necrotic center and the disintegrating periphery. Intracellular retention of COL10 and MATN3 was calculated by dividing the total green fluorescence intensity of the area co-staining with PDI (red) by the total green fluorescence intensity of the whole image. The ER size was quantified from the average area of PDI fluorescence.

Transmission electron microscopy (TEM)

On day 56 of HI, pellets were PBS washed and fixed in 2.5% glutaraldehyde for 8 hours at 4°C. After PBS washing and post-fixation in 2% osmium tetroxide for 2 hours, the pellets were dehydrated and embedded in Quetol 812 resin. 1 μm sections were taken and stained with toluidine blue. Ultra-thin sections (120 nm) were taken and stained on grids with uranyl acetate and lead citrate. Images were taken using the H-7500 transmission electron microscope (Hitachi) with the NanoSprint500 (AMT).

Supplemental References

1. Ran FA, Hsu PD, Wright J, Agarwala V, Scott DA, Zhang F. Genome engineering using the CRISPR-Cas9 system. *Nat Protoc.* 2013;8(11):2281-2308.
2. Wataya T, Ando S, Muguruma K, Ikeda H, Watanabe K, Eiraku M, Kawada M, Takahashi J, Hashimoto N, Sasai Y. Minimization of exogenous signals in ES cell culture induces rostral hypothalamic differentiation. *Proc Natl Acad Sci U S A.* 2008;105(33):11796-801.
3. Matsuda M, Yamanaka Y, Uemura M, Osawa M, Saito MK, Nagahashi A, Nishio M, Guo L, Ikegawa S, Sakurai S, Kihara S, Maurissen TL, Nakamura M, Matsumoto T, Yoshitomi H, Ikeya M, Kawakami N, Yamamoto T, Woltjen K, Ebisuya M, Toguchida J, Alev C. Recapitulating the human segmentation clock with pluripotent stem cells. *Nature.* 2020;580(7801):124-129.
4. Umeda K, Zhao J, Simmons P, Stanley E, Elefanty A, Nakayama N. Human chondrogenic paraxial mesoderm, directed specification and prospective isolation from pluripotent stem cells. *Sci Rep.* 2012;2:455.
5. Smyth GK. Linear models and empirical bayes methods for assessing differential expression in microarray experiments. *Stat Appl Genet Mol Biol.* 2004;3:Article3.